

## ATCA SURVEY OF AMMONIA IN THE GALACTIC CENTER: THE TEMPERATURES OF DENSE GAS CLUMPS BETWEEN Sgr A\* AND Sgr B2

JÜRGEN OTT<sup>1</sup>, AXEL WEIß<sup>2</sup>, LISTER STAVELEY-SMITH<sup>3</sup>, CHRISTIAN HENKEL<sup>2,4</sup>, AND DAVID S. MEIER<sup>5,1</sup>

<sup>1</sup> National Radio Astronomy Observatory, P.O. Box O, 1003 Lopezville Road, Socorro, NM 87801, USA; [jott@nrao.edu](mailto:jott@nrao.edu)

<sup>2</sup> Max-Planck-Institut für Radioastronomie, Auf dem Hügel 69, D-53121 Bonn, Germany; [aweiss@mpifr-bonn.mpg.de](mailto:aweiss@mpifr-bonn.mpg.de), [chenkel@mpifr-bonn.mpg.de](mailto:chenkel@mpifr-bonn.mpg.de)

<sup>3</sup> International Centre for Radio Astronomy Research, The University of Western Australia,

35 Stirling Highway, Crawley, WA 6009, Australia; [Lister.Staveley-Smith@uwa.edu.au](mailto:Lister.Staveley-Smith@uwa.edu.au)

<sup>4</sup> Astronomy Department, Faculty of Science, King Abdulaziz University, P.O. Box 80203, Jeddah, Saudi Arabia

<sup>5</sup> New Mexico Institute of Mining and Technology, 801 Leroy Place, Socorro, NM 87801, USA; [dmeier@nmt.edu](mailto:dmeier@nmt.edu)

Received 2013 October 18; accepted 2014 February 16; published 2014 March 25

### ABSTRACT

We present a large-scale, interferometric survey of ammonia (1, 1) and (2, 2) toward the Galactic center observed with the Australia Telescope Compact Array. The survey covers  $\Delta\ell \sim 1^\circ$  ( $\sim 150$  pc at an assumed distance of 8.5 kpc) and  $\Delta b \sim 0.2$  ( $\sim 30$  pc) which spans the region between the supermassive black hole Sgr A\* and the massive star forming region Sgr B2. The resolution is  $\sim 20''$  ( $\sim 0.8$  pc) and emission at scales  $\gtrsim 2''$  ( $\gtrsim 3.2$  pc) is filtered out due to missing interferometric short spacings. Consequently, the data represent the denser, compact clouds and disregards the large-scale, diffuse gas. Many of the clumps align with the 100 pc dust ring and mostly anti-correlate with 1.2 cm continuum emission. We present a kinetic temperature map of the dense gas. The temperature distribution peaks at  $\sim 38$  K with a width at half maximum between 18 K and 61 K (measurements sensitive within  $T_{\text{kin}} \sim 10\text{--}80$  K). Larger clumps are on average warmer than smaller clumps which suggests internal heating sources. Our observations indicate that the circumnuclear disk  $\sim 1.5$  pc around Sgr A\* is supplied with gas from the  $20 \text{ km s}^{-1}$  molecular cloud. This gas is substantially cooler than gas  $\sim 3\text{--}15$  pc away from Sgr A\*. We find a strong temperature gradient across Sgr B2. Ammonia column densities correlate well with SCUBA  $850 \mu\text{m}$  fluxes, but the relation is shifted from the origin, which may indicate a requirement for a minimum amount of dust to form and shield ammonia. Around the Arches and Quintuplet clusters we find shell morphologies with UV-influenced gas in their centers, followed by ammonia and radio continuum layers.

*Key words:* Galaxy: center – ISM: clouds – ISM: kinematics and dynamics – ISM: molecules – ISM: structure – stars: formation

*Online-only material:* color figures

### 1. INTRODUCTION

With a distance of only 8.5 kpc (IAU value used throughout the manuscript, but see Reid et al. 2009, who derive  $\sim 8.0$  kpc) the Galactic center is obviously by far the most nearby core of a massive galaxy. It is dominated by a large Galactic bar potential ( $\sim 4.5$  kpc half-length; Cabrera-Lavers et al. 2008) and hosts a  $\sim 4 \times 10^6 M_\odot$  supermassive black hole (Ghez et al. 2008; Gillessen et al. 2009). The area is at the center of the Galactic gravitational potential and exhibits some of the most complex and energetic processes in our Milky Way. The bar forces gas from the disk to be funneled to the center via  $x_1$  and  $x_2$  orbits (e.g., Stark et al. 2004; Kim et al. 2011). Within the bar potential, most of the molecular gas resides in a  $\sim 500$  pc region dubbed the Central Molecular Zone (CMZ; e.g., Morris & Serabyn 1996; Oka et al. 1998; Jones et al. 2012) and can be considered the region where  $x_2$  orbits dominate (e.g., Rodriguez-Fernandez et al. 2006). The cloud trajectories in the bar potential are self-intersecting which results in a large number of cloud–cloud collisions. The collisions induce shocks that dominate the physical and chemical properties of the interstellar matter (ISM) in the region, in particular the molecular gas. The shocks inject turbulence into the gas and are a potential heating sources. Turbulence is measured by the increased line widths of the molecular gas in the Galactic center region, with values typically of tens of  $\text{km s}^{-1}$  whereas giant molecular clouds in the disk of the Milky Way exhibit line widths of only a few  $\text{km s}^{-1}$ .

Cloud–cloud collisions also influence the properties of star formation in the region. Studies (e.g., Alexander et al. 2007; Bartko et al. 2010; Lu et al. 2013) find that the initial mass function in the central parts of the Galactic center region is skewed toward massive stars more than elsewhere in the Local Universe. In addition, the sheer amount and density of molecular material (about a few percent, or a few  $10^7 M_\odot$ , of all molecular gas in the Milky Way is concentrated in about 0.01% of the volume) coupled with a star formation rate of  $\sim 0.1 M_\odot \text{ yr}^{-1}$  (e.g., Crocker et al. 2011) produces a large number of high mass stars. Through stellar evolution, they inject mechanical power of  $\sim 10^{40} \text{ erg s}^{-1}$  in the form of strong stellar winds and supernovae, and return about  $0.02 M_\odot$  of material back to the ISM (for an overview, see Crocker et al. 2011). A dramatic effect of these energy sources might be the  $\sim 10^\circ$  sized *Fermi* bubbles that extend perpendicular to the Galactic disk far into the Galaxy’s halo (e.g., Su et al. 2010; Crocker et al. 2011; Carretti et al. 2013). The high density and short lifetimes of the massive stars also produce many compact, energetic objects and the CMZ is under the influence of a large flux of UV and X-ray photons as well as cosmic rays that can penetrate the molecular gas. Some of these sources influence gas locally, others influence gas on larger scales. Overall, however, the state of the gas in the CMZ is dominated by shock physics (e.g., Martín-Pintado et al. 2000; Martín et al. 2008; Protheroe et al. 2008; Amo-Baladrón et al. 2009).

Given all local and global influences, it is important to understand how star formation can proceed under these conditions.

The molecular gas defines the site and the material for star formation and it is an important goal to directly measure the parameters of the molecular gas such as temperature, density, turbulence, ionization fraction, and magnetic field penetration. In this paper we concentrate on the temperature of the gas. Our goal is to produce a temperature map of the Galactic center gas, in particular of the denser gas phase on parsec scales that match the size of the individual star formation locations. A comparison of the temperatures with nearby sources, and a correlation with the cloud properties will allow us to derive the most likely heating sources of the gas, and whether they are external or internal to the gas clouds.

We decide to use ammonia as a temperature tracer. Ammonia ( $\text{NH}_3$ ) has a peculiar structure of a prolate symmetric top, a tetrahedron with a nitrogen atom in one corner and three hydrogen atoms in the remaining corners. The nitrogen atom can tunnel through the plane defined by the three hydrogen atoms. This possibility removes the degeneracy of the symmetric top levels ( $J, K$ ) at  $J > 0$ , which splits the energy levels into doublets. Transitions between those levels can be measured as “inversion lines.” The inversion line frequencies directly depend on the rotational states of the molecule. By measuring the intensity of an inversion line one can thus derive the number of  $\text{NH}_3$  molecules at the given rotational state. The population interchange between different  $K$  ladders is solely governed by collisions, and all ( $J > K, K$ ) states decay fast into the metastable  $J = K$  levels. The distribution of all ( $J, J$ ) states is thus a result of the energetics of the collisions, and is simply described by a Boltzmann distribution at a temperature  $T$ . Ammonia is thus an excellent thermometer.

In the following we present interferometric observations of the ammonia (1, 1) and (2, 2) transitions across a large fraction in the CMZ which we use to construct a temperature map of the clumped gas in the region at pc size resolution. The observations and data reduction are described in Section 2, followed by our results in Section 3. A discussion of the morphology, kinematics, temperature structure of the gas clumps and their relation to other Galactic center objects are presented in Section 4, followed by a summary in Section 5.

## 2. OBSERVATIONS AND DATA REDUCTION

### 2.1. General Setup

We observed the Galactic center during eight nights on 2005 August 3–8, 10, and 12 with the Australia Telescope Compact Array (ATCA,<sup>6</sup> project id: C 1322) with five antennas in the most compact, hybrid H 75 array configuration (baselines in the range of 31 to 89 m). Antenna CA 06 was also used but, due to the long baselines to the rest of the array ( $\sim 4.5$  km), it is down-weighted and does not contribute substantially to the surface brightness sensitivity.

The  $K$ -band system at the ATCA was tuned to observe both polarizations at a center frequency of 23.708 GHz with a bandwidth of 64 MHz split into 128 channels. This setup was chosen to observe both, the  $\text{NH}_3$  (1, 1) (rest frequency: 23.6945 GHz) and (2, 2) (rest frequency: 23.7226 GHz) lines simultaneously within the same band (when adjusting for the systemic velocity of the Galactic center and the observatory velocity at the time of the observations). This resulted in a velocity resolution of  $\sim 6.3$  km s<sup>-1</sup> at a total local standard of

rest (LSR) velocity range of  $-180$  to  $+165$  km s<sup>-1</sup> common to both lines.

Given that the shortest baseline is 31 m, the array is only sensitive to emission less extended than  $\sim 1/3$ , which corresponds to about half the primary beam of the observations ( $\sim 2/4$ ).

### 2.2. Mosaicking Technique

Our survey covers an area of  $0.2$  deg<sup>2</sup>,  $1^\circ$  in Galactic longitude ( $-0^\circ.2 \leq \ell \leq 0^\circ.8$ ) and  $0^\circ.2$  in Galactic latitude ( $-0^\circ.13 \leq b \leq 0^\circ.07$ ), i.e., it is centered on  $\ell = 0^\circ.3$  and  $b = 0^\circ.03$ . At the assumed distance of the Galactic center, 8.5 kpc, the covered area corresponds to widths of  $\sim 148$  pc in  $\ell$  and  $\sim 30$  pc in  $b$ ,  $\sim 4440$  pc<sup>2</sup> in total.

A hexagonal, fully sampled pointing pattern was used to cover the observed area (primary  $K$ -band beam of the ATCA:  $\sim 2/4$ ), 840 pointings in total. To obtain the most uniform  $uv$ -coverage we set up the following mosaicking strategy: The field was split up into six different, equal-sized sub-regions along Galactic longitude, with 140 pointing centers each. In addition, each sub-region was furthermore split up into two different scans, each of which covers half (i.e., 70 pointings) of the area: an  $\ell$  scan along Galactic longitude and a  $b$  scan along Galactic latitude (see Figure 1). Scans of the fields were started at different sidereal times during the eight nights making sure that each scan and field, i.e., the entire 840 pointings of the survey, are covered at least once per night and in rare occasions twice. The typical  $uv$ -coverage of a single pointing is shown in the bottom panel of Figure 1. Note, however, that due to our distinct  $\ell$  and  $b$  scan driving scheme and the overlaps of the primary beams in the hexagonal pattern, the actual  $uv$ -coverage at any position on the map is better.

Each pointing has an integration time of  $\sim 30$  s per night, accumulating to  $\sim 4$  minutes in total. Time lost between the pointings due to acceleration and deceleration of the ATCA dishes for our survey amounts to about a second and is therefore negligible.

### 2.3. Calibration

Flux calibration was performed using daily observations of the ATCA standard calibrator PKS 1934–638. The  $\sim 1.3$  Jy bright phase (complex gain) calibrator PKS 1710–269 was observed twice for 2 minutes each  $\ell$  or  $b$  scan, i.e., every  $\sim 35$  minutes (see Section 2.2). PKS 1710–269 is located at the Galactic coordinates  $\ell = 357^\circ.73044774$ ,  $b = 6^\circ.99364372$  and can be considered to be a point source for this array configuration and frequency. The same source was used to update the pointing of the individual ATCA antennas every  $\sim 1.5$  hr with typical corrections of  $\sim 5''$ . Antenna-based bandpasses were determined by daily  $\sim 10$  minute integrations on PKS 1255–055 (also known as 3C279), which has a flux of  $\sim 15$  Jy in  $K$ -band. We estimate the absolute flux uncertainty to  $\sim 15\%$ . Note, however, that both ammonia lines were observed in the same band. Relative flux values and resulting parameters such as the temperature (Section 4.4) are therefore much more accurate.

All data reduction steps were performed with the *MIRIAD* software package (Sault et al. 1995). All data were first corrected for atmospheric opacity (task *atlod* with option *opcorr*) and edited for corrupt visibilities and shadowed antennas. Furthermore, the first seven and last three edge channels were discarded. The task *mfcad* was used to obtain bandpass and complex gain solutions and *gpboot* performed absolute flux calibration. These solutions were bootstrapped to the complex gain

<sup>6</sup> The Australia Telescope Compact Array is part of the Australia Telescope which is funded by the Commonwealth of Australia for operation as a National Facility managed by CSIRO.

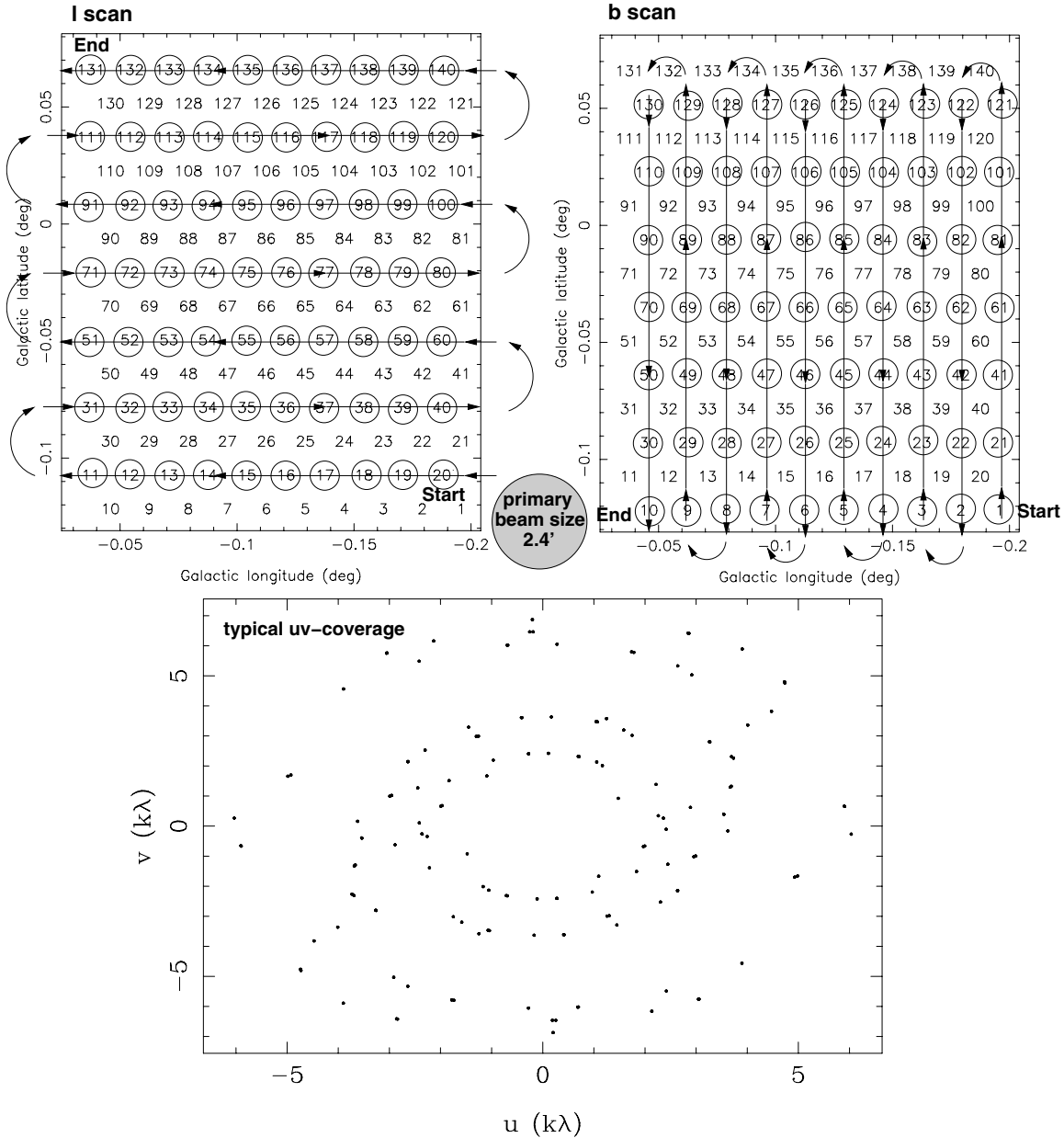


**Figure 1.** Top: Scanning pattern of the sub-mosaic fields. Every second row was scanned first in one direction and later the remaining pointings in the orthogonal direction. Each number marks a pointing center of the entire field and numbers in circles indicate those observed in the respective  $\ell$  or  $b$  scan. The primary beam size of the ATCA in  $K$ -band is  $\sim 2.4'$ , shown in between the two panels. Bottom: Typical  $uv$ -coverage for a single mosaic point.

calibrator (and eventually to the data) when the latter was at the same elevation as the flux calibrator PKS 1934–638. The 1.2 cm radio continuum was separated from the  $uv$  data using line-free channels at either end of the spectra and in between the  $\text{NH}_3$  (1, 1) and (2, 2) lines (task *uvlin*).

#### 2.4. Imaging

The task *invert* was used to Fourier transform the visibilities into a combined mosaic image of all pointings, including the corrections for the primary beam shapes. During that step the visibilities were weighted in the natural scheme as well as by the inverse of their noise variance. Eventually the data were deconvolved with the maximum entropy algorithm as implemented in *mosmem*. A first step comprised a non-restricted 30 iteration run of *mosmem* across the mosaic, followed by a

restoration of the cube (task *restor*). This cube, however, still showed considerable sidelobe structure. The results improved substantially after using the result from the first application of *mosmem*, convolving it to about twice the natural beam size, and blanking all values below 100 mJy beam<sup>-1</sup> per channel, in the following we call this cube the “mask.” Eventually, the original data set was deconvolved again, but we forced *mosmem* to only act on those pixels where the mask was non-blank. The restoration process of the resulting new deconvolved model with the residuals of the deconvolution process did eventually preserve the fluxes in the maps. The effects of the sidelobes on the data, however, were drastically reduced. We checked the fluxes of the maximum entropy deconvolution with the more familiar CLEAN algorithm (task *mosstdi*) and found that while the fluxes are comparable, the extended emission was much better reproduced with *mosmem*.

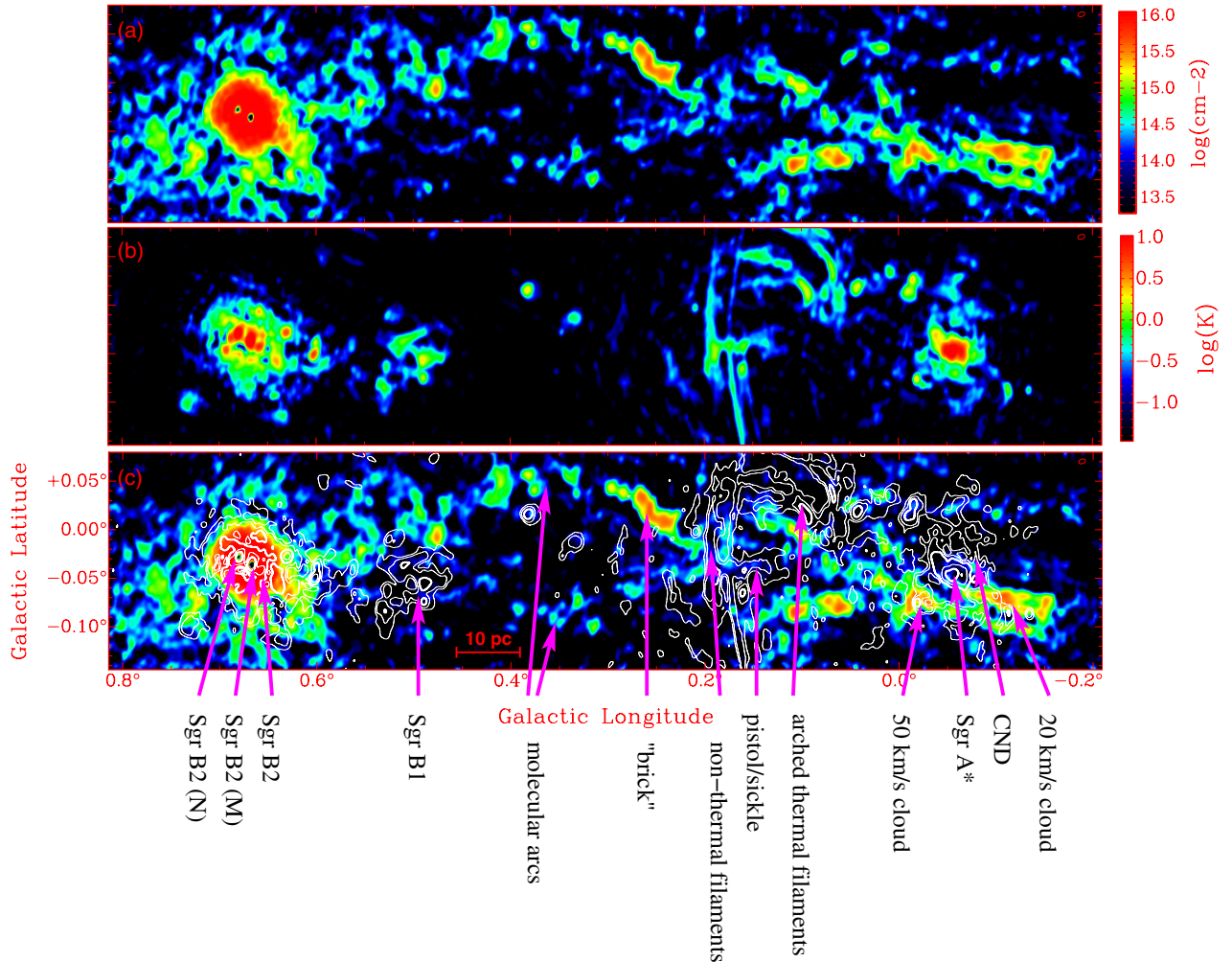


**Figure 2.** (a) Integrated intensity map of the  $\text{NH}_3$  (1, 1) emission in logarithmic units of column density. (b) Logarithmic 1.2 cm radio continuum. (c) The same figure as in (a) but with contours of the 1.2 cm continuum overlaid, the contours are in logarithmic units in the range of  $-1 \leq \log(T_{\text{mb;cont}}) \leq 1$  in steps of 0.5. The beam of the observations ( $\sim 26''.2 \times 16''.8$ , P.A. =  $-70^\circ$ ) is shown in the upper right corners.

(A color version of this figure is available in the online journal.)

The final data have a beam size of  $\sim 26''.2 \times 16''.8$ , with a position angle (P.A.) of  $-70^\circ$ , corresponding to a physical resolution in the Galactic center of  $\sim 1.1 \text{ pc} \times 0.7 \text{ pc}$ . The pixel size of the data was chosen to be  $4''$ . The flux rms noise per channel is  $\sim 7 \text{ mJy beam}^{-1}$  which corresponds to an rms brightness of  $\sim 35 \text{ mK}$ .

Eventually, the total data cube was split into cubes that comprise only the  $\text{NH}_3$  (1, 1) or the  $\text{NH}_3$  (2, 2) inversion lines.

### 3. RESULTS

#### 3.1. Radio Continuum

Using the line-free channels from our data, we are also able to construct a 1.2 cm continuum map which is displayed in Figure 2(b). The dynamic range across all pointings of the mosaic is of order  $10^4$  with the brightest sources toward Sgr A\* at  $T_{\text{mb}} = 30.5 \text{ K}$  (with some confusion from close-by sources), and Sgr B2 (M) and (N) with main beam brightness temperatures of 48.5 K and 27.9 K, respectively. The “mini-spiral” associated with Sgr A\* is also visible as is the Sgr B1 region at  $(\ell, b) \approx (0^\circ 49, -0^\circ 06)$ . Some of the most striking features are the presence of the non-thermal radio arcs along

Galactic longitudes of  $\ell \sim 0^\circ 18$ . Their fluxes increase from high to low latitudes from  $\sim 0.2$  to  $\sim 0.6 \text{ K}$  with the brightest,  $\sim 1.4 \text{ K}$  spots in the “pistol” or “sickle” region at  $(\ell, b) = (0^\circ 189, -0^\circ 051)$  (see Figure 2; for a spectral index analysis, see Lang et al. 1999). The thin, unresolved vertical filaments appear to be connected in projection to the thermal, arched filaments that start at  $b \approx 0.07$  and extend to  $(\ell, b) \approx (0^\circ 071, -0^\circ 001)$ . Between that position and the Sgr A\* region, a number of scattered radio continuum point sources are detected in the map. Overall, the 1.2 cm ATCA radio continuum map exhibits a very similar morphology when compared to the 21 cm and 90 cm Very Large Array maps presented by Yusef-Zadeh et al. (2004), Anantharamaiah et al. (1991), and Nord et al. (2004). The low frequency maps, however, also contain a number of finer, arcminute long filaments, perpendicular to the plane, sometimes called non-thermal radio filaments or threads, that we do not detect in our 1.2 cm data.

#### 3.2. Sample Spectra

In Figure 3 we show spectra from the ammonia datacubes at different positions in the CMZ. The measured parameters of Gaussian fits to the spectra are listed in Table 1 and derived

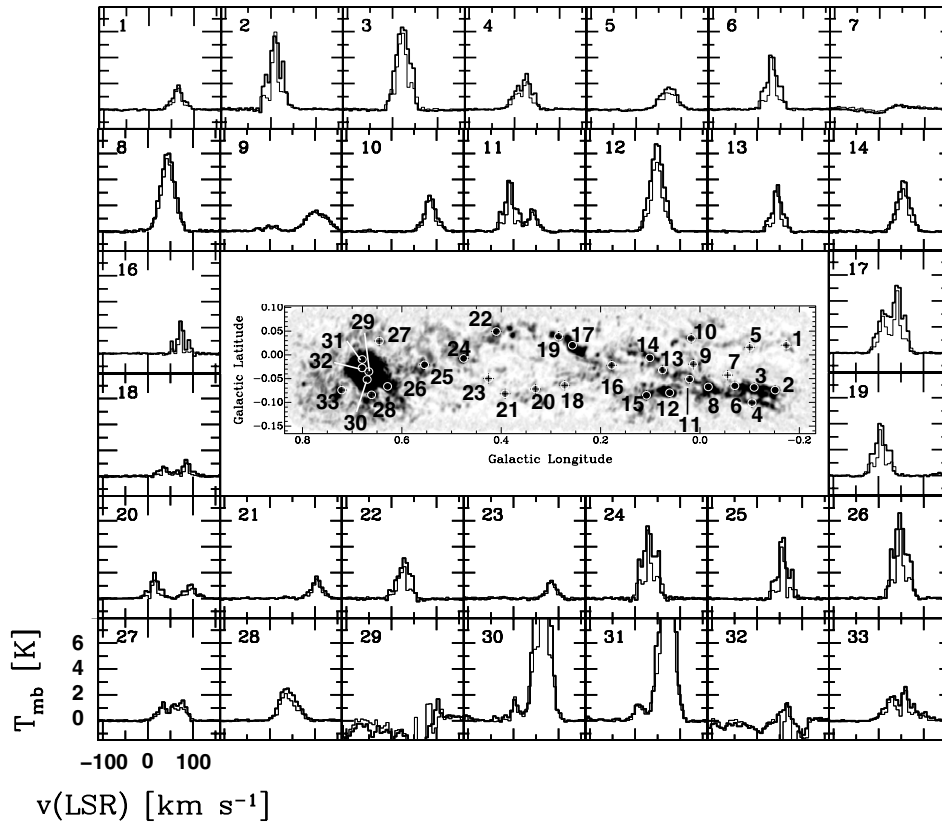


**Figure 3.** Ammonia spectra toward individual positions. The numbers in the spectral panels correspond to the positions in the map. All spectra are at the same scale.  $\text{NH}_3$  (1, 1) is displayed in thick and  $\text{NH}_3$  (2, 2) in thin lines. The parameters of the spectra are listed in Tables 1 and 2.

values in Table 2. For better orientation, we also indicate the area that the positions belong to in Figure 3. Ammonia (1, 1) peak brightness temperatures are typically around  $\sim 1$  K with values of up to  $\sim 17$  K.  $\text{NH}_3$  (2, 2) peak temperatures are typically  $\sim 10\%$  weaker than those of the (1, 1) line. FWHM widths of the sample spectra are  $20\text{--}40$   $\text{km s}^{-1}$ . Some of the positions show multiple ammonia components and are listed with “a” and “b” appendices in the tables. Ammonia has hyperfine structure which needs to be distinguished from multiple gas components and also adds to the FWHM. An analysis is presented in Section 3.6.

Absorption is observed toward the star forming regions Sgr B2 (N) at position 32, Sgr B2 (M) at position 29, and the supermassive black hole Sgr A\* at position 7. The absorption spectra are rather complex and contain all components along the lines of sight from the earth to the CMZ.

### 3.3. Total Intensity

The integrated ammonia (1, 1) intensity map is shown in Figure 2. In this representation, the velocity integrated brightness temperature was converted to  $\text{NH}_3$  (1, 1) column densities. The upper level column of the inversion line can be derived via the following relation:

$$N_u(J, K) = \frac{7.77 \times 10^{13}}{\nu} \frac{J(J+1)}{K^2} \int T_{\text{mb}} dv \quad (1)$$

(Henkel et al. 2000) where  $N_u$  is given in units of  $\text{cm}^{-2}$ , the frequency  $\nu$  in GHz, the main beam brightness temperature  $T_{\text{mb}}$  in K, and the velocity  $v$  in  $\text{km s}^{-1}$ . The upper and lower levels of each inversion line are almost evenly populated due to the small energy difference. We therefore double each upper level

population to arrive at the total, upper, and lower population for each line.

The dynamic range of the map spans more than two orders of magnitude with the Sgr B2 molecular cloud being exceptionally bright. In fact, the interferometric map around Sgr B2 shows a very steep gradient with a decline in brightness by a factor of  $\sim 30$  within a radius of only 5 pc (for a more detailed discussion of the profile see Protheroe et al. 2008). Part of the steep decline, however, might be due to the missing short spacings which filters out very extended emission (Section 2). Single dish maps (e.g., Guesten et al. 1981; Handa et al. 2006; Purcell et al. 2012) show extremely bright and extended emission, so the short spacing filtering effect is substantial in this region and we detect only the local peaks of the emission. Toward the positions of Sgr B2 (M) and (N) at  $(0^\circ:667, -0^\circ:036)$  and  $(0^\circ:680, -0^\circ:029)$ , respectively, the ultra-compact H II regions (see also Figure 2(b)) are bright enough in the radio continuum to yield ammonia absorption instead of emission. This explains the two “holes” on top of this region.

Very striking features are the two “molecular arcs” in between Sgr B2 and a Galactic longitude of  $\sim 0^\circ:2$ . The molecular arcs appear to be symmetric with the symmetry axis slightly below the zero Galactic latitude line at  $b \sim -0^\circ:02$ ; one arc spanning up to  $b \sim 0^\circ:06$  and the other up to  $b \sim -0^\circ:09$  (outlined by the dashed and dotted lines in Figure 4). If they are coherent features, they have lengths of  $\sim 0^\circ:5$  which corresponds to  $\sim 75$  pc. They are mostly coincident with the dusty ring detected as a cold structure in *Herschel* temperature maps by Molinari et al. (2011; see also Section 4.3). One of the brightest clumps being part of the molecular arcs is the “brick” G0.253+0.016 at  $(0^\circ:253, 0^\circ:016)$ . It is a high density, compact molecular clump with an integrated brightness temperature of  $\sim 230$   $\text{K km s}^{-1}$

**Table 1**  
Parameters Derived from Gaussian Fits to the Sample Spectra

No.	$\ell$ (deg)	$b$ (deg)	$T_{\text{mb,peak}}^{11}$ (K)	$v_{\text{LSR,peak}}^{11}$ (km s <sup>-1</sup> )	$\Delta v_{\text{FWHM}}^{11}$ (km s <sup>-1</sup> )	$\int_{11} T_{\text{mb}} dv$ (K km s <sup>-1</sup> )	$T_{\text{mb,peak}}^{22}$ (K)	$v_{\text{LSR,peak}}^{22}$ (km s <sup>-1</sup> )	$\Delta v_{\text{FWHM}}^{22}$ (km s <sup>-1</sup> )	$\int_{22} T_{\text{mb}} dv$ (K km s <sup>-1</sup> )
1	-0.173	0.020	1.68 ± 0.05	64.31 ± 0.39	27.79 ± 0.91	49.61 ± 2.16	1.56 ± 0.08	64.67 ± 0.45	18.66 ± 1.06	31.02 ± 2.32
2	-0.151	-0.074	5.47 ± 0.55	8.37 ± 1.37	28.00 ± 3.23	163.05 ± 24.91	5.80 ± 0.36	9.26 ± 0.42	13.50 ± 0.97	83.41 ± 7.97
3	-0.109	-0.069	6.42 ± 0.13	22.90 ± 0.35	37.05 ± 0.83	253.46 ± 7.54	5.19 ± 0.20	21.72 ± 0.58	30.75 ± 1.37	170.05 ± 10.03
4	-0.105	-0.101	2.31 ± 0.08	22.04 ± 0.78	43.80 ± 1.84	107.52 ± 5.96	1.62 ± 0.08	20.73 ± 1.02	41.58 ± 2.41	71.82 ± 5.50
5	-0.100	0.016	1.72 ± 0.04	72.29 ± 0.44	42.54 ± 1.04	78.11 ± 2.52	1.24 ± 0.04	71.77 ± 0.70	42.46 ± 1.65	56.29 ± 2.89
6	-0.070	-0.065	3.75 ± 0.12	31.79 ± 0.52	32.20 ± 1.23	128.56 ± 6.48	4.01 ± 0.21	31.59 ± 0.37	14.57 ± 0.89	62.24 ± 4.99
8	-0.017	-0.067	6.06 ± 0.04	44.30 ± 0.13	37.68 ± 0.29	243.15 ± 2.51	5.26 ± 0.08	44.17 ± 0.24	34.17 ± 0.57	191.47 ± 4.25
9a	0.013	-0.020	0.37 ± 0.03	0.47 ± 1.87	47.65 ± 4.45	18.92 ± 2.33	0.30 ± 0.04	-0.72 ± 3.64	48.68 ± 9.01	15.30 ± 3.67
9b			1.56 ± 0.04	104.79 ± 0.64	57.24 ± 1.53	94.92 ± 3.33	1.43 ± 0.04	103.69 ± 0.70	54.99 ± 1.65	83.85 ± 3.31
10	0.018	0.035	2.65 ± 0.04	85.96 ± 0.24	30.67 ± 0.57	86.56 ± 2.14	2.39 ± 0.07	85.07 ± 0.36	23.57 ± 0.85	60.08 ± 2.86
11a	0.021	-0.051	3.47 ± 0.14	-7.58 ± 0.62	30.67 ± 1.51	113.34 ± 7.26	3.71 ± 0.22	-7.58 ± 0.62	12.54 ± 0.85	49.49 ± 4.46
11b			1.62 ± 0.16	42.96 ± 1.20	25.04 ± 2.92	43.14 ± 6.53	1.11 ± 0.13	42.96 ± 1.20	36.71 ± 5.03	43.24 ± 7.81
12	0.061	-0.080	6.69 ± 0.06	48.66 ± 0.16	35.30 ± 0.37	251.47 ± 3.49	5.09 ± 0.12	48.34 ± 0.35	29.47 ± 0.83	159.68 ± 5.97
13	0.075	-0.032	3.23 ± 0.10	45.27 ± 0.40	26.44 ± 0.93	90.87 ± 4.25	3.33 ± 0.13	44.92 ± 0.26	13.52 ± 0.64	47.98 ± 3.00
14	0.101	-0.006	3.78 ± 0.05	54.71 ± 0.22	33.77 ± 0.52	136.05 ± 2.75	2.96 ± 0.09	53.96 ± 0.43	29.27 ± 1.00	92.33 ± 4.18
15	0.108	-0.085	7.15 ± 0.11	52.06 ± 0.28	35.80 ± 0.66	272.62 ± 6.61	6.13 ± 0.20	51.56 ± 0.49	31.44 ± 1.16	205.18 ± 10.02
16	0.178	-0.022	2.45 ± 0.18	73.04 ± 0.56	15.19 ± 1.32	39.64 ± 4.54	2.93 ± 0.37	71.86 ± 0.42	6.61 ± 0.84	20.65 ± 3.69
17a	0.257	0.020	2.96 ± 0.17	8.04 ± 1.26	26.86 ± 2.64	84.54 ± 9.58	2.49 ± 0.19	11.84 ± 0.96	24.07 ± 2.47	63.73 ± 8.18
17b			4.86 ± 0.15	43.20 ± 0.84	30.99 ± 1.86	160.22 ± 10.78	4.40 ± 0.24	41.73 ± 0.43	14.63 ± 1.02	68.62 ± 6.06
18a	0.272	-0.064	0.62 ± 0.05	36.50 ± 1.49	36.13 ± 3.71	23.68 ± 3.13	0.68 ± 0.08	37.08 ± 0.62	9.77 ± 1.45	7.03 ± 1.36
18b			1.17 ± 0.07	85.72 ± 0.61	20.84 ± 1.45	25.87 ± 2.33	1.03 ± 0.07	85.56 ± 0.43	9.40 ± 0.71	10.33 ± 1.07
19	0.284	0.039	3.62 ± 0.12	5.79 ± 0.56	34.57 ± 1.32	133.31 ± 6.71	2.40 ± 0.17	5.66 ± 1.12	31.29 ± 2.64	79.91 ± 8.90
20a	0.331	-0.072	1.67 ± 0.10	15.37 ± 0.78	25.90 ± 1.84	46.08 ± 4.33	1.50 ± 0.10	14.91 ± 0.40	11.79 ± 0.94	18.84 ± 1.99
20b			1.00 ± 0.06	93.98 ± 0.86	30.43 ± 2.04	32.32 ± 2.86	0.62 ± 0.07	95.48 ± 1.71	30.50 ± 4.03	20.15 ± 3.52
21	0.392	-0.082	1.52 ± 0.04	104.80 ± 0.40	29.40 ± 0.95	47.70 ± 2.05	1.36 ± 0.05	104.63 ± 0.37	20.92 ± 0.87	30.37 ± 1.68
22	0.410	0.049	2.95 ± 0.09	28.09 ± 0.49	33.58 ± 1.15	105.41 ± 4.78	2.16 ± 0.11	25.04 ± 0.62	24.10 ± 1.47	55.38 ± 4.47
23	0.425	-0.050	1.35 ± 0.04	84.86 ± 0.38	25.91 ± 0.89	37.15 ± 1.69	1.28 ± 0.07	84.69 ± 0.56	20.76 ± 1.33	28.37 ± 2.39
24	0.475	-0.007	4.99 ± 0.23	31.73 ± 0.84	37.66 ± 1.97	200.15 ± 13.84	3.05 ± 0.25	32.17 ± 1.48	36.91 ± 3.49	119.81 ± 14.96
25	0.554	-0.021	4.01 ± 0.21	57.59 ± 0.73	28.76 ± 1.73	122.97 ± 9.76	4.63 ± 0.33	56.72 ± 0.27	9.71 ± 0.86	47.91 ± 5.43
26	0.629	-0.066	5.87 ± 0.20	47.59 ± 0.61	37.16 ± 1.44	232.15 ± 11.86	3.58 ± 0.23	47.94 ± 1.06	33.74 ± 2.50	128.71 ± 12.62
27a	0.645	0.029	1.17 ± 0.07	31.94 ± 1.26	28.45 ± 2.89	35.42 ± 4.20	1.04 ± 0.09	31.94 ± 1.26	22.78 ± 2.26	25.14 ± 3.27
27b			1.51 ± 0.07	71.31 ± 1.04	31.83 ± 2.48	51.10 ± 4.59	1.04 ± 0.07	71.31 ± 1.04	39.10 ± 3.27	43.21 ± 4.52
28	0.661	-0.084	2.48 ± 0.04	40.67 ± 0.40	45.72 ± 0.93	120.65 ± 3.26	1.90 ± 0.05	39.53 ± 0.56	40.40 ± 1.31	81.67 ± 3.50
30a	0.670	-0.052	1.48 ± 0.32	4.13 ± 2.17	20.18 ± 5.13	31.71 ± 10.65	1.79 ± 0.96	4.01 ± 3.28	11.19 ± 6.49	21.34 ± 16.88
30b			16.92 ± 0.25	64.12 ± 0.25	34.55 ± 0.59	622.43 ± 13.95	15.20 ± 0.67	65.64 ± 0.57	26.65 ± 1.35	431.38 ± 28.88
31a	0.680	-0.010	1.34 ± 0.39	7.53 ± 3.16	21.73 ± 7.51	30.91 ± 14.04	1.23 ± 0.39	8.35 ± 3.23	20.70 ± 7.65	27.02 ± 13.18
31b			11.09 ± 0.28	70.01 ± 0.53	42.52 ± 1.28	502.07 ± 19.77	10.18 ± 0.28	70.50 ± 0.53	38.87 ± 1.27	421.59 ± 18.10
33a	0.721	-0.074	0.87 ± 0.13	28.19 ± 1.07	48.93 ± 7.83	45.49 ± 9.88	1.64 ± 0.14	28.18 ± 1.07	25.39 ± 2.71	44.27 ± 6.02
33b			1.48 ± 0.12	58.55 ± 0.45	63.72 ± 5.05	100.27 ± 11.28	2.64 ± 0.21	58.55 ± 0.45	11.84 ± 1.18	33.23 ± 4.21

**Notes.** Whenever two velocity components could be distinguished, they are labeled “a” and “b” ( $\ell/b$ : Galactic longitude/latitude in B1950 coordinates;  $T_{\text{mb,peak}}$ : peak brightness temperature;  $v_{\text{LSR,peak}}$ : peak LSR velocity;  $\Delta v_{\text{FWHM}}$ : FWHM velocity width, superscripts distinguish between the (1, 1) and the (2, 2) inversion transition lines).

that could be the formation site of a massive star cluster (e.g., Longmore et al. 2012).

The sightline toward Sgr A\* is relatively weak with a temperature-velocity integral of  $\sim 11.7$  K km s<sup>-1</sup>. At distances of  $\sim 30''$  from Sgr A\* however, we do see surrounding emission from the circumnuclear disk (CND), a feature that is also prominent in lines of other molecules such as HCN (Christopher et al. 2005; Montero-Castaño et al. 2009, see Section 4.6 for details).

Toward negative Galactic longitudes, the 20 km s<sup>-1</sup> cloud at  $(\ell, b) \sim (-0.1, -0.08)$  is one of the strongest features in our map and it splits into three almost parallel filaments with lengths of  $\sim 0.1$  or  $\sim 15$  pc. The two at higher  $b$  are with 110–130 K km s<sup>-1</sup> very similar in integrated brightness, whereas the one at lower  $b$  is somewhat weaker with 80–100 K km s<sup>-1</sup>.

In between the 20 km s<sup>-1</sup> cloud and the molecular arcs is the region where the massive Arches and Quintuplet clusters reside (see Section 4.5). In that part of the CMZ, the molecular arcs intersect in projection, giving way to a somewhat rounder, shell-

like structure. This structure is located near to a large cloud that is elongated perpendicular to the Galactic plane in the vicinity of the non-thermal radio continuum arc (Section 3.1). From there, two molecular features are visible that form a “>” shape and merge close to the 20 km s<sup>-1</sup> cloud.

### 3.4. Global Velocity Structure

Binning three channels to velocity widths of  $\sim 19$  km s<sup>-1</sup>, the channel maps of the ammonia (1, 1) and (2, 2) inversion line emission are displayed in Figures 5 and 6, respectively. As expected, the NH<sub>3</sub> (2, 2) emission is generally somewhat fainter but very similar in structure to the (1, 1) emission. Given the dynamic range of the data (see Section 3.3), we display the maps in logarithmic units. At low velocities, the tip of the 20 km s<sup>-1</sup> cloud as well as the molecular arc at  $b > 0^\circ$  are visible (see also Figure 2). The southern molecular arc breaks up into clouds at velocities  $\sim 20$  km s<sup>-1</sup> and  $\sim 80$  km s<sup>-1</sup> and is therefore not as coherent in velocity space as the northern one. It is somewhat

**Table 2**

Derived Parameters of the Sample Spectra ( $N(1, 1)$ ,  $N(2, 2)$ : Ammonia Column Densities of the (1, 1) and (2, 2) Lines;  $N_{\text{tot}}$ : Total Column Density for the Traced Ammonia Component;  $T_{\text{rot},12}$ : Rotational Temperatures Based on (1, 1) and (2, 2);  $T_{\text{kin}}$ : Kinetic Temperatures)

No.	Nearby GC Feature	$N(1, 1)$ ( $10^{14} \text{ cm}^{-2}$ )	$N(2, 2)$ ( $10^{14} \text{ cm}^{-2}$ )	$N_{\text{tot}}$ ( $10^{14} \text{ cm}^{-2}$ )	$T_{\text{rot},12}$ (K)	$T_{\text{kin}}$ (K)
1	Dust ring north of Sgr A*	$6.50 \pm 0.28$	$3.04 \pm 0.22$	$15.4 \pm 1.56$	$32 \pm 2$	$43^{+5}_{-4}$
2	20 km s <sup>-1</sup> cloud	$21.38 \pm 3.26$	$8.20 \pm 0.78$	$48.78 \pm 16.8$	$28 \pm 2$	$32^{+5}_{-4}$
3	20 km s <sup>-1</sup> cloud	$33.24 \pm 0.98$	$16.70 \pm 0.98$	$80.28 \pm 5.66$	$34 \pm 2$	$48^{+5}_{-5}$
4	20 km s <sup>-1</sup> cloud	$14.10 \pm 0.78$	$7.06 \pm 0.54$	$34.00 \pm 4.46$	$34 \pm 2$	$47^{+6}_{-6}$
5	Dust ring north of Sgr A*	$10.24 \pm 0.34$	$5.54 \pm 0.28$	$25.34 \pm 1.98$	$37 \pm 2$	$55^{+6}_{-5}$
6	20 km s <sup>-1</sup> cloud	$16.86 \pm 0.84$	$6.12 \pm 0.250$	$38.24 \pm 4.34$	$27 \pm 2$	$31^{+3}_{-3}$
7	Sgr A*	...	...	...	...	...
8	50 km s <sup>-1</sup> cloud	$31.90 \pm 0.32$	$18.82 \pm 0.42$	$81.84 \pm 2.14$	$40 \pm 1$	$66^{+5}_{-4}$
9a	Arched thermal filaments	$2.48 \pm 0.30$	$1.50 \pm 0.36$	$6.44 \pm 1.96$	$41 \pm 5$	$70^{+\infty}_{-17}$
9b	Arched thermal filaments	$12.46 \pm 0.44$	$8.24 \pm 0.32$	$33.88 \pm 3.16$	$45 \pm 2$	$89^{+\infty}_{-10}$
10	Arched thermal filaments	$11.36 \pm 0.28$	$5.90 \pm 0.28$	$27.72 \pm 1.64$	$35 \pm 2$	$51^{+5}_{-5}$
11a	50 km s <sup>-1</sup> cloud	$14.86 \pm 0.96$	$4.86 \pm 0.44$	$33.50 \pm 4.84$	$25 \pm 2$	$28^{+3}_{-3}$
11b	50 km s <sup>-1</sup> cloud	$5.66 \pm 0.86$	$4.24 \pm 0.76$	$16.70 \pm 6.96$	$52 \pm 6$	$137^{+\infty}_{-42}$
12	South of the clusters	$32.98 \pm 0.46$	$15.7 \pm 0.58$	$78.38 \pm 2.56$	$33 \pm 1$	$44^{+3}_{-3}$
13	Arched thermal filaments	$11.92 \pm 0.56$	$4.72 \pm 0.30$	$27.30 \pm 2.90$	$29 \pm 2$	$34^{+3}_{-3}$
14	Arched thermal filaments	$17.84 \pm 0.36$	$9.08 \pm 0.42$	$43.24 \pm 2.08$	$35 \pm 1$	$49^{+4}_{-4}$
15	South of the clusters	$35.76 \pm 0.86$	$20.16 \pm 0.98$	$90.00 \pm 5.38$	$38 \pm 2$	$60^{+6}_{-6}$
16	Non-thermal arcs	$5.20 \pm 0.60$	$2.02 \pm 0.36$	$11.88 \pm 3.08$	$28 \pm 3$	$33^{+6}_{-5}$
17a	Brick	$11.08 \pm 1.26$	$6.26 \pm 0.80$	$27.92 \pm 7.68$	$38 \pm 3$	$60^{+13}_{-11}$
17b	brick	$21.02 \pm 1.42$	$6.74 \pm 0.60$	$47.32 \pm 7.18$	$25 \pm 2$	$27^{+3}_{-3}$
18a	Southern mol. arc	$3.10 \pm 0.42$	$0.70 \pm 0.14$	$7.14 \pm 2.24$	$20 \pm 2$	$20^{+3}_{-2}$
18b	Southern mol. arc	$3.40 \pm 0.30$	$1.02 \pm 0.10$	$7.64 \pm 1.56$	$24 \pm 2$	$25^{+3}_{-3}$
19	Northern mol. arc	$17.48 \pm 0.88$	$7.86 \pm 0.88$	$40.98 \pm 4.74$	$31 \pm 2$	$40^{+5}_{-5}$
20a	Southern mol. arc	$6.04 \pm 0.56$	$1.86 \pm 0.20$	$13.60 \pm 2.88$	$24 \pm 2$	$26^{+3}_{-3}$
20b	Southern mol. arc	$4.24 \pm 0.38$	$1.98 \pm 0.34$	$10.02 \pm 2.04$	$32 \pm 3$	$42^{+8}_{-7}$
21	Southern mol. arc	$6.26 \pm 0.26$	$2.98 \pm 0.16$	$14.88 \pm 1.50$	$33 \pm 2$	$44^{+5}_{-4}$
22	Northern mol. arc	$13.82 \pm 0.62$	$5.44 \pm 0.44$	$31.64 \pm 3.26$	$29 \pm 2$	$34^{+4}_{-3}$
23	Southern mol. arc	$4.88 \pm 0.22$	$2.78 \pm 0.24$	$12.34 \pm 1.38$	$39 \pm 2$	$62^{+9}_{-8}$
24	Northern mol. arc	$26.26 \pm 1.82$	$11.78 \pm 1.48$	$61.50 \pm 9.76$	$31 \pm 2$	$40^{+6}_{-5}$
25	Tip of mol. arc	$16.14 \pm 1.28$	$4.70 \pm 0.54$	$36.32 \pm 6.54$	$24 \pm 2$	$25^{+3}_{-2}$
26	Sgr B2 area	$30.46 \pm 1.56$	$12.64 \pm 1.24$	$70.26 \pm 8.18$	$30 \pm 2$	$36^{+4}_{-4}$
27a	Sgr B2 area	$4.64 \pm 0.56$	$2.46 \pm 0.32$	$11.44 \pm 3.22$	$36 \pm 3$	$53^{+11}_{-9}$
27b	Sgr B2 area	$6.70 \pm 0.60$	$4.24 \pm 0.44$	$17.80 \pm 4.08$	$43 \pm 3$	$79^{+\infty}_{-14}$
28	Sgr B2 area	$15.82 \pm 0.42$	$8.02 \pm 0.34$	$38.32 \pm 2.48$	$35 \pm 1$	$49^{+5}_{-4}$
29	Sgr B2 (M)	...	...	...	...	...
30a	Sgr B2 area	$4.16 \pm 1.40$	$2.10 \pm 1.66$	$10.06 \pm 7.68$	$34 \pm 13$	$48^{+58}_{-26}$
30b	Sgr B2 area	$81.64 \pm 1.84$	$42.38 \pm 2.84$	$199.22 \pm 10.70$	$35 \pm 2$	$51^{+6}_{-5}$
31a	Sgr B2 area	$4.06 \pm 1.84$	$2.66 \pm 1.30$	$10.96 \pm 3.00$	$44 \pm 15$	$87^{+\infty}_{-52}$
31b	Sgr B2 area	$64.86 \pm 2.60$	$41.42 \pm 1.78$	$174.36 \pm 17.74$	$42 \pm 2$	$77^{+\infty}_{-9}$
32	Sgr B2 (N)	...	...	...	...	...
33a	Sgr B2 area	$5.96 \pm 1.30$	$4.34 \pm 0.60$	$17.24 \pm 10.04$	$50 \pm 6$	$123^{+\infty}_{-40}$
33b	Sgr B2 area	$13.16 \pm 1.48$	$3.26 \pm 0.42$	$29.86 \pm 7.78$	$22 \pm 2$	$22^{+2}_{-2}$

**Note.** Note that for rotational temperatures of 40 K and above, only lower limits to the kinetic temperature >80 K can be derived.

surprising that this arc does not have many cloud components in the intermediate velocity range at  $\sim 50 \text{ km s}^{-1}$ . The molecular gas at ( $\ell < 0^\circ$ ,  $b > 0^\circ$ ) is in the velocity range of  $50\text{--}100 \text{ km s}^{-1}$  with an additional component at  $\sim -60$  to  $-40 \text{ km s}^{-1}$ . The intensity-weighted velocity map (moment 1; Figure 4) indicates a very similar velocity structure in the ( $\ell < 0^\circ$ ,  $b > 0^\circ$ ) region and the arc structure at negative  $b$  values between Sgr A\* and Sgr B2. Note that emission at negative velocities is relatively

weak and thus the intensity-weighted velocity map displayed in Figure 4(b) is biased toward larger values.

In Figure 7 we show a position-velocity map of the entire data cube. The grayscale is the peak intensity determined along  $b$ . In this plot the velocity difference between the different molecular arcs becomes apparent again, with a maximum separation of  $\sim 100 \text{ km s}^{-1}$  and an indication that the tips of the arcs arrive at similar velocities after a smooth velocity difference decrease.

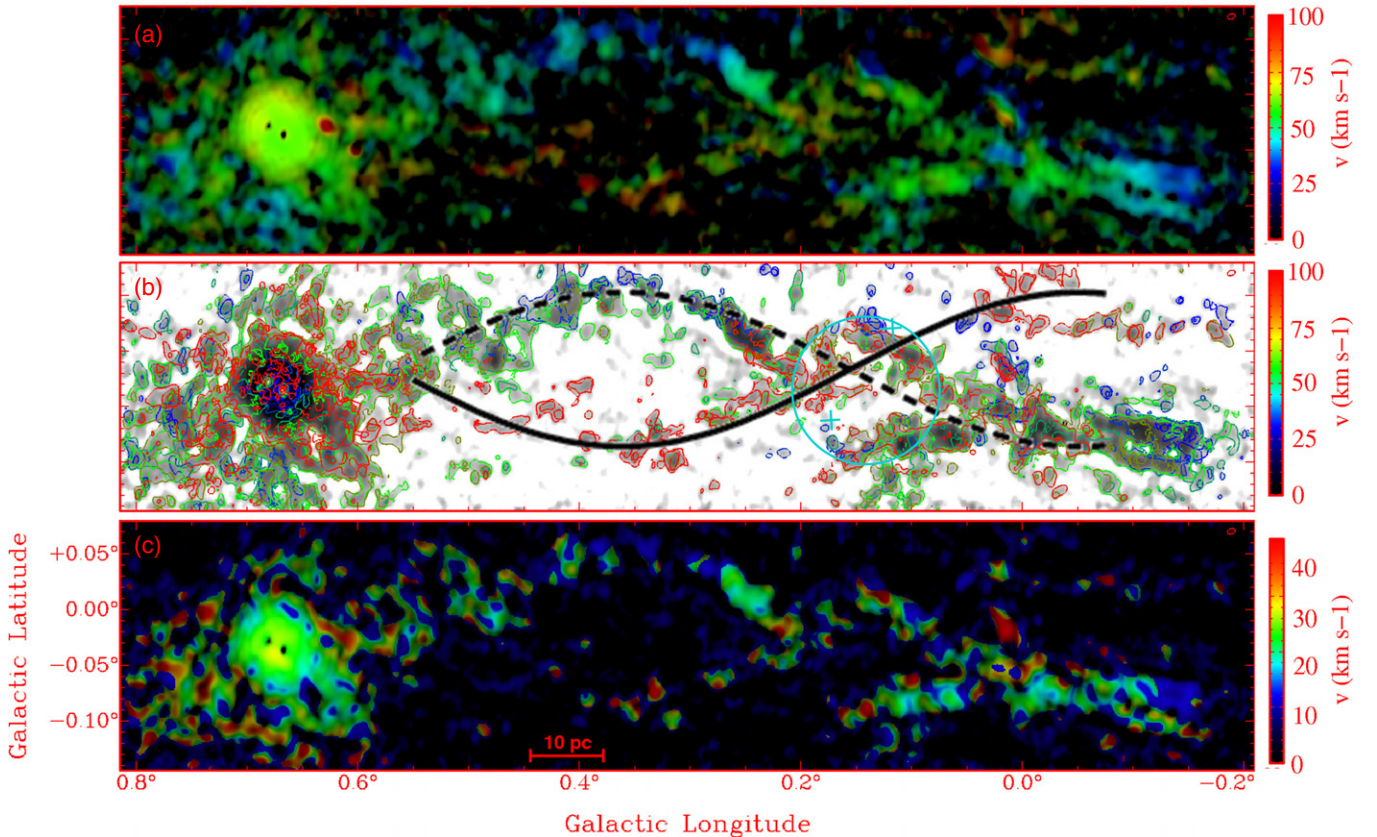


**Figure 4.** Velocity structure as colors projected on the integrated emission. (a) Intensity-weighted mean velocity map (first moment). (b) An intensity contour per plane of the  $\text{NH}_3$  (1, 1) emission data cube, color coded by velocity (sometimes referred to as a “renzogram”). The plot is overlaid on the integrated emission and we indicate two symmetric cosine functions that roughly describe the pattern of the molecular arcs. These features likely delineate the “100 pc” ring. The solid curve describes the molecular arc in the foreground and the dashed curve indicates the arc in the background. The cyan circle denotes a possible cavity close to the site of the Arches and Quintuplet clusters, both clusters are marked as cyan crosses. (c) velocity dispersion (moment 2). Note that double line spectra may show up as artificially high velocity dispersions and also affect the mean velocities.

(A color version of this figure is available in the online journal.)

The mean velocity of Sgr B2 is about  $\sim 70 \text{ km s}^{-1}$  and absorption of ammonia toward Sgr A\* is at  $\sim 0 \text{ km s}^{-1}$ . Despite local deviations, a trend can be observed for velocities to decrease from large  $\ell$  toward Sgr A\*. This trend may be extended to the other directions. The  $20 \text{ km s}^{-1}$  cloud, for example, is closer to Sgr A\* than the  $50 \text{ km s}^{-1}$  cloud which itself is closer to the Center of the Galaxy than Sgr B2 at  $70 \text{ km s}^{-1}$ . The velocity decline toward Sgr A\* may indicate streaming motions along the central bar of the Galaxy (e.g., Blitz & Spergel 1991), or an  $x_2$  orbit along the 100 pc dust ring described by Molinari et al. (2011) (see also Section 4.3). In the first case, if we take the angle of the Galactic bar with respect to the Sun–Sgr A\* line of  $22^\circ$  (Babusiaux & Gilmore 2005), we derive a velocity gradient of the molecular gas at the de-projected distance of Sgr B2 ( $\sim 270 \text{ pc}$ ) of  $\sim 75 \text{ km s}^{-1}$  along the bar toward Sgr A\* (projected, i.e., measured distance and velocity:  $\sim 100 \text{ pc}$  and  $\sim 70 \text{ km s}^{-1}$ ). This corresponds to an average velocity gradient of  $\sim 0.28 \text{ km s}^{-1} \text{ pc}^{-1}$ . The dynamic timescale for Sgr B2 gas streaming along the bar toward the Galactic center would therefore be  $\sim 3.5 \text{ Myr}$  in this picture. If Sgr B2 is on the 100 pc ring (see Section 4.3), it will take  $\sim 2 \text{ Myr}$  to reach a position that is aligned in projection with Sgr A\*.

The line widths of the ammonia emission are in the range of  $20\text{--}40 \text{ km s}^{-1}$  without significant differences toward individual regions (see Table 1). In Figure 2 we show the second moment of the ammonia (1, 1) data cube. The very large values in this map, however, are at positions with multiple line components

and do not reflect the true velocity dispersions of the ammonia distribution.

### 3.5. Temperature Map

One of the main goals of this survey is to derive a temperature map of the region between Sgr A\* and Sgr B2. As alluded to in the introduction, the ratio of the upper level populations  $N_u$  for two different inversion lines,  $(J', J')$  and  $(J, J)$ , can be expressed by a rotational temperature  $T_{\text{rot}}$ . This parameter can be derived via the following equation

$$\frac{N_u(J', J')}{N_u(J, J)} = \frac{g_{\text{op}}(J') 2J' + 1}{g_{\text{op}}(J) 2J + 1} \exp\left(\frac{-\Delta E}{T_{\text{rot}, J' J'}}\right), \quad (2)$$

(e.g., Ott et al. 2005).  $\Delta E$  is the energy difference between the  $\text{NH}_3(J', J')$  and the  $\text{NH}_3(J, J)$  levels in  $K$  [41.2 K between  $\text{NH}_3(1, 1)$  and  $(2, 2)$ ],  $g_{\text{op}}$  are the statistical weights given as  $g_{\text{op}} = 1$  for both para-ammonia (1, 1) and (2, 2) inversion transitions. Large velocity gradient (LVG) radiative transfer models (e.g., Ott et al. 2005) show that the population distribution (and thus the temperature) is almost entirely independent of the density of the gas, and the above relation can be used for densities that start at the critical density of ammonia of  $\sim 10^3 \text{ cm}^{-3}$  up to extreme densities of  $\sim 10^7 \text{ cm}^{-3}$ .

For low temperatures, the rotational temperatures correspond well to kinetic temperatures. At higher energies, however, collisional de-excitation and the dependency of the collisional

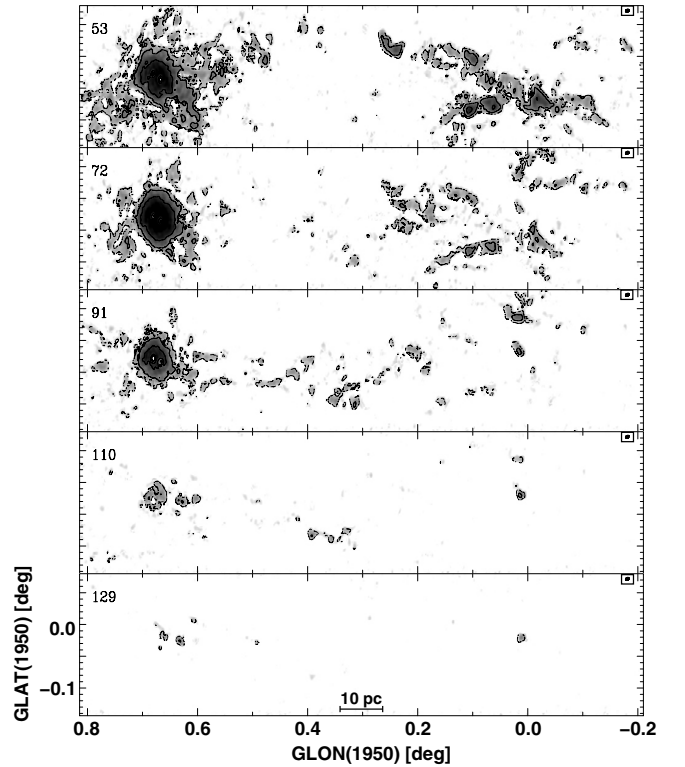
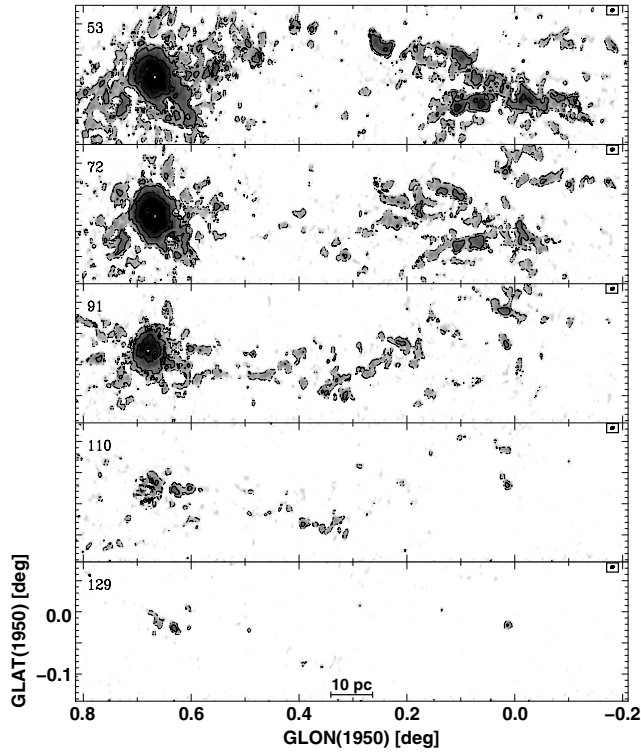
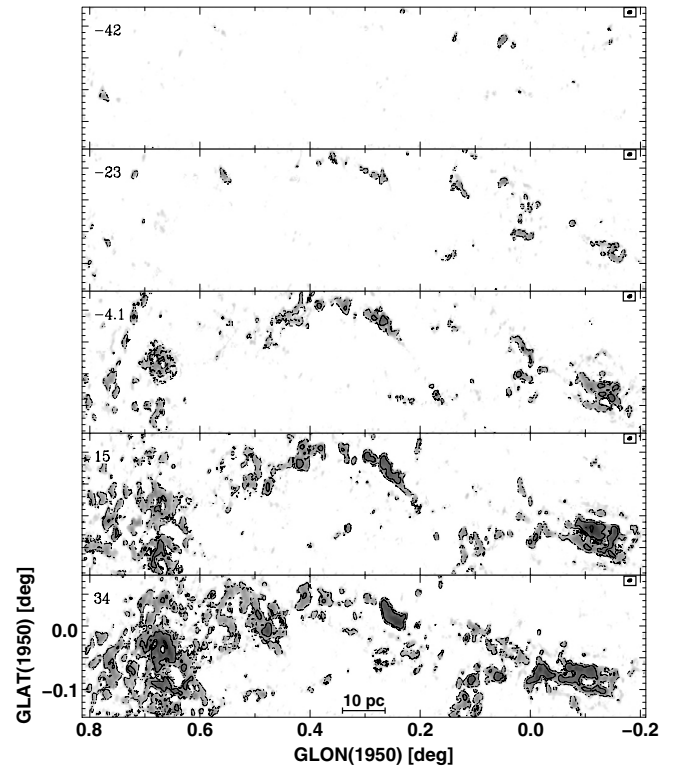
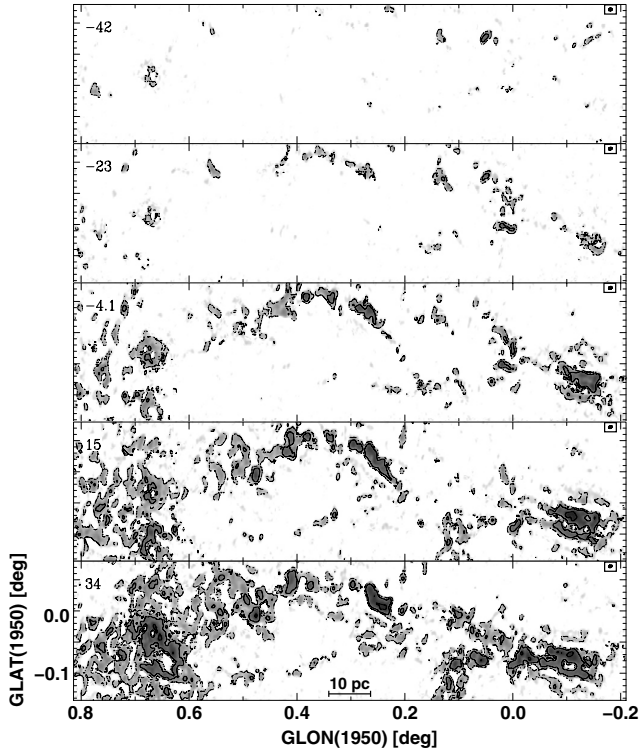


**Figure 5.** Channel maps of the  $\text{NH}_3(1, 1)$  emission in logarithmic units of  $T_{\text{mb}}$  (grayscale ranges:  $-1.0 \leq \log(T_{\text{mb}}[\text{K}]) \leq 1.0$ , contours are at  $\log(T_{\text{mb}}[\text{K}])$  values of  $-0.6$ ,  $0$ , and  $+0.6$ ). Each panel comprises three binned channels with mean LSR velocities in  $\text{km s}^{-1}$  shown in the upper left corners, and the synthesized beam ( $\sim 26''.2 \times 16''.8$ , P.A. =  $-70^\circ$ ) in the upper right corners.

cross-section on the energy result in a deviation from this trend. LVG calculations suggest that the equation

$$T_{\text{kin}} = 6.06 \times \exp(0.061 T_{\text{rot},12}) \quad (3)$$

**Figure 6.** Channel maps of the  $\text{NH}_3(2, 2)$  emission in logarithmic units of  $T_{\text{mb}}$ . Scales, contours, and labels are the same as in Figure 5.

provides a reasonable approximation for the conversion from  $T_{\text{rot},12}$  to  $T_{\text{kin}}$  (see Figure 5 in Ott et al. 2011). The relation is flattening at  $T_{\text{kin}} \gtrsim 80$  K ( $T_{\text{rot},12} \sim 40$  K) and we therefore consider 80 K as the lower limit for all higher temperatures (similar calculations are shown, e.g., in Guesten et al. 1981;

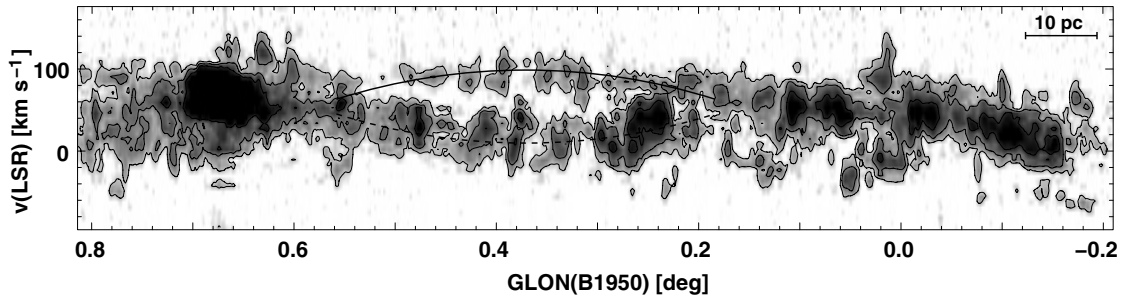


**Figure 7.** Position–velocity map of the  $\text{NH}_3$  (1, 1) emission. The data cube for this plot is collapsed across Galactic latitude and the peak intensity along that axis is shown in both grayscale and contours. The black solid and dashed lines indicate the same clouds as outlined in Figure 4(b).

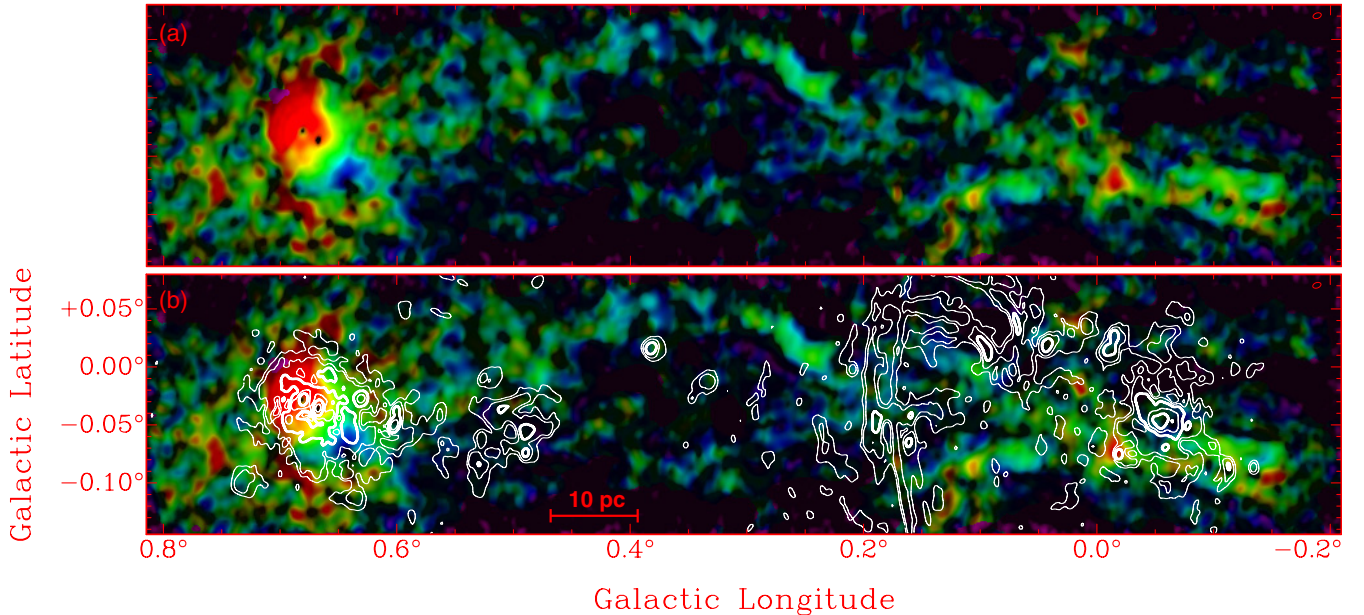


**Figure 8.** Kinetic temperature image of the Galactic center region between Sgr A\* and Sgr B2. Violet:  $T_{\text{kin}} \lesssim 25$  K, blue:  $25 \text{ K} \lesssim T_{\text{kin}} \lesssim 45$  K, green:  $45 \text{ K} \lesssim T_{\text{kin}} \lesssim 65$  K, red:  $T_{\text{kin}} \gtrsim 65$  K. In the lower panel, 1.2 cm continuum contours are overlaid with the same spacing as in Figure 2.

(A color version of this figure is available in the online journal.)

Walmsley & Ungerechts 1983; Mauersberger et al. 1986; Danby et al. 1988). To determine higher temperatures more accurately, higher  $J = K$  inversion lines need to be observed (e.g., Mills & Morris 2013).

Applying Equation (3) to our data, we construct a kinetic temperature map of the region between Sgr A\* and Sgr B2 which is displayed in Figure 8. Most of the kinetic gas temperatures, in particular in the molecular arcs between Sgr A\* and Sgr B2 are relatively uniform at  $\sim 30$  K for smaller clouds and about  $\sim 50$  K for the larger molecular complexes. Hotter molecular gas with temperatures of  $\gtrsim 80$  K are found toward clouds in the vicinity of Sgr A\* and in the Sgr B2 region. In particular, across Sgr B2 a temperature gradient is visible with temperatures exceeding 80 K at high Galactic latitude and longitude, and much colder temperatures of  $\sim 30$  K at lower Galactic latitudes and longitudes. First indications for this gradient have been described in the literature, e.g., in Churchwell & Hollis (1983) or Huttemeister et al. (1993b), but the gradient was never imaged in this lucidity before.

### 3.6. Optical Depths

As already mentioned, the lines in the observed field are, with  $\sim 20$ – $40 \text{ km s}^{-1}$ , quite broad. On the other side, our velocity

resolution of  $\sim 6.3 \text{ km s}^{-1}$  is relatively coarse. Together, both properties of the data make it difficult to determine the strength of the ammonia hyperfine lines that are  $\sim \pm 8 \text{ km s}^{-1}$  and  $\sim \pm 20 \text{ km s}^{-1}$  from the main line. However, for some relatively narrow lines it is possible to detect the hyperfine lines separately and in Figure 3 lines at positions 2, 6, 11, 19, 24, 25, and 28, do show some indications of the  $\sim \pm 20 \text{ km s}^{-1}$  hyperfine structure. For those lines the main-to-hyperfine line flux ratios are very consistent at a ratio of  $\sim 2.2$  with only  $\sim 20\%$  variation. Using

$$\frac{T_{\text{mb,peak}}(\text{main lines})}{T_{\text{mb,peak}}(\text{outer hyperfine lines})} = \frac{1 - \exp(-\tau)}{1 - \exp(-0.22\tau)} \quad (4)$$

(Ho & Townes 1983) we derive optical depths  $\tau$  to be  $\sim 2.4 \pm 1$ .

A spectral fit with the  $\text{NH}_3$  fitting routines in the CLASS software provide similar optical depths, ranging from about  $\tau \sim 1$  to  $\sim 3.5$ , with the majority in the  $\tau \sim 1.5$  to 2 range. The fits, taking into account the hyperfine line strengths, also result in line widths that are smaller than the measured ones and typically 10–20  $\text{km s}^{-1}$  less than the simple FWHM line widths.

The calculations of the column densities (Section 3.3) assume optically thin ammonia lines. A correction for the sightlines with moderate optical depths can be expressed by  $\tau/(1 - \exp[-\tau])$ .

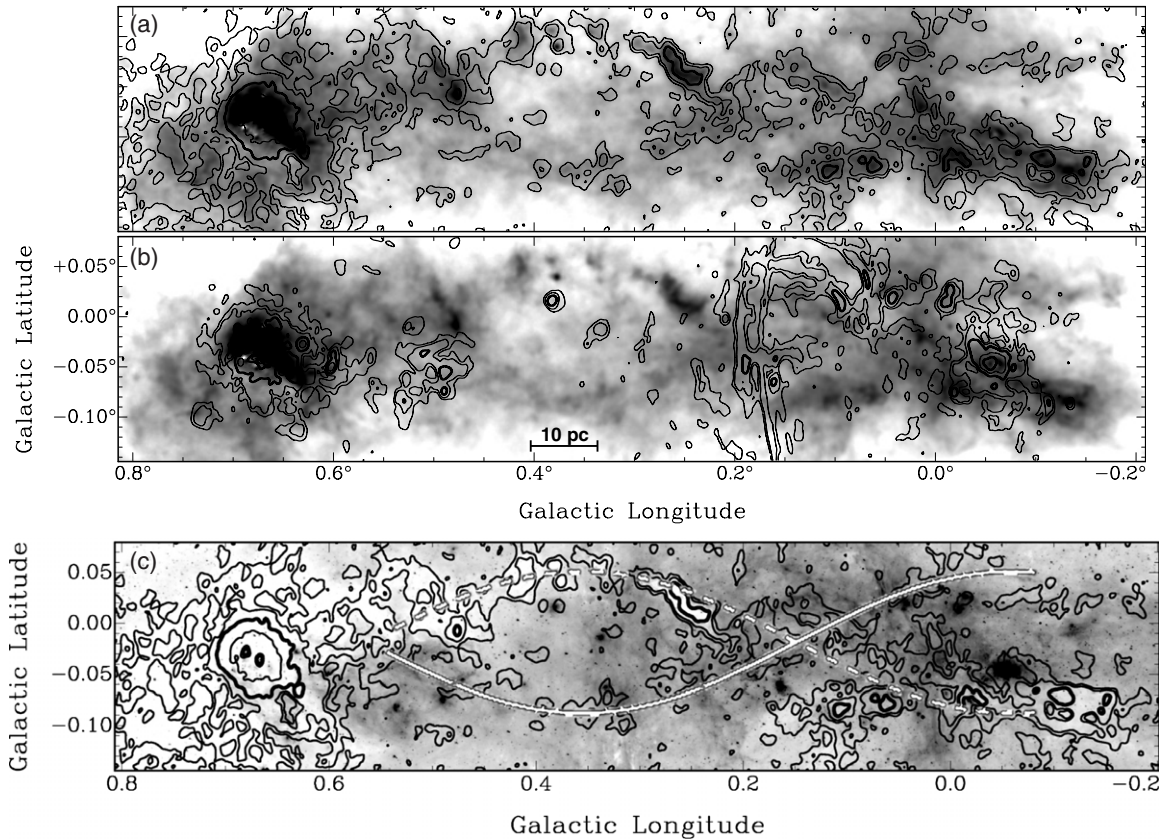


**Figure 9.** (a) SCUBA 850  $\mu\text{m}$  map in logarithmic units with the ammonia (1, 1) integrated column density overlaid. The contours are within the  $14 \leq \log(N[\text{cm}^{-2}]) \leq 15.5$  interval, spaced by  $\log(N[\text{cm}^{-2}]) = 0.5$  (b) The SCUBA map with contours of the 1.2 cm continuum spaced as in Figure 2. (c) *Spitzer* 8  $\mu\text{m}$  image in logarithmic units (taken from Arendt et al. 2008). Overlaid on this image are the ammonia (1, 1) column density contours and the dotted and dashed white lines correspond to those in Figure 4(b).

For our  $\tau \sim 1\text{--}2.4$  cases this amounts to  $\sim 1.6\text{--}2.7$ . Changes to the temperature, however, are minimal and the correction factors cancel out (Equation (2)) when the optical depths for the (1, 1) and (2, 2) lines are identical. This is in fact a good assumption since the average temperatures of the gas is at  $\sim 38$  K (see Section 4.4, see also Section 3.5), which is in between the energies above ground for the (1, 1) [ $E = 22.7$  K] and (2, 2) [ $E = 63.9$  K] levels, respectively. In the unlikely edge cases where one of the transitions is optically thin and the other exhibits  $\tau \sim 2$ , any temperature corrections would also be close to a factor of  $\sim 2$ , with colder temperatures for higher optical depths of the (1, 1) line.

## 4. DISCUSSION

### 4.1. Comparison to SCUBA observations

In Figure 9 we show ammonia (1, 1) column density contours overlaid on a SCUBA 850  $\mu\text{m}$  map. The absolute flux of the SCUBA data is somewhat uncertain due to the chopping technique used (see Pierce-Price et al. 2000, for a description of the original data) and should be treated as a lower limit since extended flux is likely filtered out. As mentioned in Section 2.2, our interferometric ammonia measurements suffer from similar problems and a short spacing correction with single dish data would be required to recover the entire flux of the region. Therefore, on large scales, the comparison of extended emission in both maps will not be very reliable. On more compact scales, on which this paper focuses, however, the data can be compared and the ammonia (1, 1) column densities and the SCUBA

850  $\mu\text{m}$  data trace each other extremely well. All features, except for Sgr A\* and the ammonia absorption against the compact H II regions Sgr B2(N) and (M) are reproduced in both datasets. Sgr A\* is dominated by non-thermal emission (e.g., Liu & Melia 2001) and is therefore unrelated to dusty molecular gas.

To determine the validity of a dust-to-gas relationship between ammonia and the SCUBA 850  $\mu\text{m}$  data, we determined both fluxes in each pixel ( $4''$  in size) after smoothing to a common resolution of  $30''$ . Following this, we binned the distribution of the pixels in the  $\text{NH}_3$  (1, 1) column density versus the SCUBA 850  $\mu\text{m}$  fluxes in order to obtain a point density distribution of these values. The logarithmically scaled point density distribution is shown in Figure 10. The tips of the contours (largest values in dust and gas) follow an almost linear relation as indicated by the dashed line. The line, however, is not centered on the origin of the plot but shifted along the SCUBA 850  $\mu\text{m}$  axis. This offset may be the result of the missing large scale flux of both maps. However, if the 850  $\mu\text{m}$  flux is underestimated, the line would shift even further away from the origin on this axis. On the other hand, if it is mainly the interferometric ammonia measurements where we miss flux, the graph would shift up and could be brought in agreement with starting at the origin. But such a shift would be extreme as a correction of  $\sim 2 \times 10^{15} \text{ cm}^{-2}$  is required, a value that would almost double the column density for an average cloud (taking account missing SCUBA flux will increase the difference even further). Temperature variations of gas and dust are unlikely to have a significant effect on the slope of the plot, but could broaden the distribution. We also

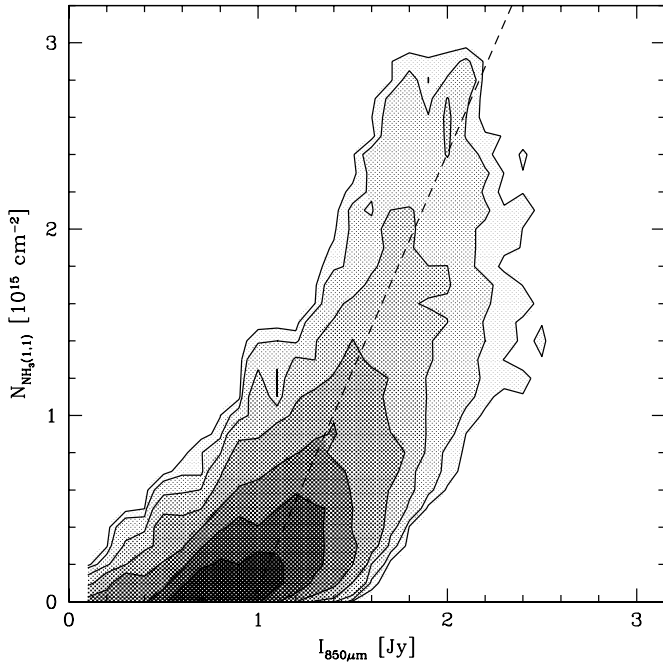


**Figure 10.** Contour plot of the SCUBA 850  $\mu\text{m}$  fluxes against the  $\text{NH}_3(1, 1)$  column densities per pixel at  $30''$  resolution, excluding Sgr A\* and Sgr B2. Shown are the contours of the point densities in logarithmic units. The tips of the contours can be described by an almost linear relationship as is indicated by the dashed line.

corrected for the temperature and calculated *total* ammonia column densities from the (1, 1) line and the temperature (via the Equation (A15) in Ungerechts et al. 1986). As listed in Table 2, the (1, 1) and (2, 2) populations are together about half of the total ammonia column density that we derive from our data. A comparison with the entire ammonia column density thus leads to a very similar plot as the one shown in Figure 10 and it does not contain a substantial additive component. In addition, 850  $\mu\text{m}$  dust fluxes are not exceedingly susceptible to variations in temperature. The offset of the line may thus be due to a large amount of missing flux from extended emission mainly of the  $\text{NH}_3(1, 1)$  line. A different explanation for the offset would be that the ammonia forms on dust grains which also shields the material and that a minimum of dust is required to produce ammonia efficiently and to protect it against destruction through the surrounding UV radiation field (see also the discussion in Weiß et al. 2001).

#### 4.2. The Radio Filaments and the Molecular Gas

In contrast to the SCUBA maps, the radio continuum emission and the molecular gas as traced by ammonia show little coincidence. Only the star forming region Sgr B2 exhibits radio continuum emission from the H II regions at the same positions where large amounts of molecular gas are found (see Figure 2). For this region it is obvious that the molecular gas most likely feeds the current star forming activity. As already noted by Mehringer et al. (1995), there is much less molecular gas in the star forming Sgr B1 region at  $(\ell, b) = (0^\circ:50, -0^\circ:05)$ . This may indicate that the Sgr B1 region is more evolved than Sgr B2 and that the remaining molecular gas has already been dispersed.

In addition, the non-thermal radio arcs at  $\ell \sim 0.15$  also occupy a region with only little ammonia line emission. The pistol/sickle region at  $(0^\circ:16, -0^\circ:06)$ , for example, exhibits  $\text{NH}_3(1, 1)$  column densities of only  $\sim 2 \times 10^{13} \text{ cm}^{-2}$ . In addition, at larger Galactic latitudes, the radio arc bifurcates

into two roughly parallel components at  $\ell \sim 0^\circ:19$  and  $\ell \sim 0^\circ:17$ . Along the filaments, the  $\text{NH}_3(1, 1)$  column densities are  $\sim 12 \times 10^{14} \text{ cm}^{-2}$ , whereas the column density in the very thin, long area in between the two filaments rises up to  $\sim 28 \times 10^{13} \text{ cm}^{-2}$ . The radio emission in the two arched thermal filaments that connect to the main non-thermal arcs and that stretch from  $(0^\circ:14, 0^\circ:05)$  to  $(0^\circ:08, 0^\circ:00)$  and from  $(0^\circ:10, 0^\circ:08)$  to  $(0^\circ:06, 0^\circ:02)$  are also in regions with low  $\text{NH}_3$  average column densities. Toward lower Galactic latitude and lower Galactic longitudes, however, very prominent molecular gas clumps are apparent in the integrated intensity maps (cf. Figure 2). A notable exception to this behavior is the “handle” of the pistol/sickle, the radio filament that extends roughly perpendicular to the large non-thermal radio arcs at Galactic latitudes of  $\sim -0^\circ:04$ . Molecular gas appears to be aligned with this feature and exhibits column densities of  $\sim 2.4 \times 10^{14} \text{ cm}^{-2}$ . Finally, the region around Sgr A\* with the associated mini-spiral is also very bright in 1.2 cm radio continuum emission but has only weak features of molecular gas. In particular, the very prominent circumnuclear, molecular ring around Sgr A\*, which is very bright in HCN (Christopher et al. 2005), is not exceptionally strong in the  $\text{NH}_3(1, 1)$  and (2, 2) transitions (see Section 4.6). The ammonia feature has a somewhat larger diameter than that of HCN and column densities of  $2\text{--}4 \times 10^{14} \text{ cm}^{-2}$ . This is up to an order of magnitude less than the column densities in the 20 and 50  $\text{km s}^{-1}$  clouds. The more isolated radio continuum regions at  $(-0^\circ:013, 0^\circ:021)$  and  $(-0^\circ:053, 0^\circ:020)$  also show local peaks in the ammonia distribution of a few  $10^{14} \text{ cm}^{-2}$ . Associated star formation may thus be in a relatively early stage.

#### 4.3. The Molecular Arcs and the 100 pc Dust Ring

Some of the most prominent features in the interferometric ammonia map (Figure 2) are the two molecular arcs west of Sgr B2, between  $\ell \approx 0^\circ:2$  and  $0^\circ:6$ . The two Galactic northern and southern arcs are almost symmetric in shape, mirrored along a line at constant  $b \approx -0^\circ:02$ . The northern arc is certainly much brighter than the low- $b$  counterpart. In Figure 9(c) we show an overlay of the ammonia to *Spitzer* 8  $\mu\text{m}$  data. Some of the detected gas corresponds very well to strong absorption features in the infrared images. In particular the northern arc is heavily absorbing the infrared emission whereas the southern arc is hardly visible in the *Spitzer* image at all. Similarly, the string of molecular clouds north of Sgr A\* are less absorbing than those south of Sgr A\*, namely the 20 and 50  $\text{km s}^{-1}$  clouds. This can be interpreted such that the northern arc and the clouds south of Sgr A\* are in front of most of the IR emission whereas the southern arc and the clouds north of Sgr A\* are located behind. The different structures are indicated by the sinusoidal solid (back structure) and dashed (front) lines in Figure 4(b) (also in Figure 7). This picture is consistent with the morphology of the “Figure 8” 100 pc ring that was recently detected in a *Herschel* temperature map by Molinari et al. (2011). The shapes of the dust ring and our ammonia arcs are very similar and the ammonia may thus be emitted by clumps residing in the dust ring.

Molinari et al. (2011) claim that the ring is rotating, based on single dish data of the CS molecule. Our data is filtering out the diffuse emission and the clumps seem to follow a somewhat different picture. Whereas the Molinari et al. (2011) interpretation suggests that the foreground arc east of Sgr A\* should be redshifted compared to the background arc, we find the opposite. In Figure 7 the northern, foreground arc (dashed line), is at lower velocities compared the foreground arc (solid line). The velocities of the two arcs are less distinct toward

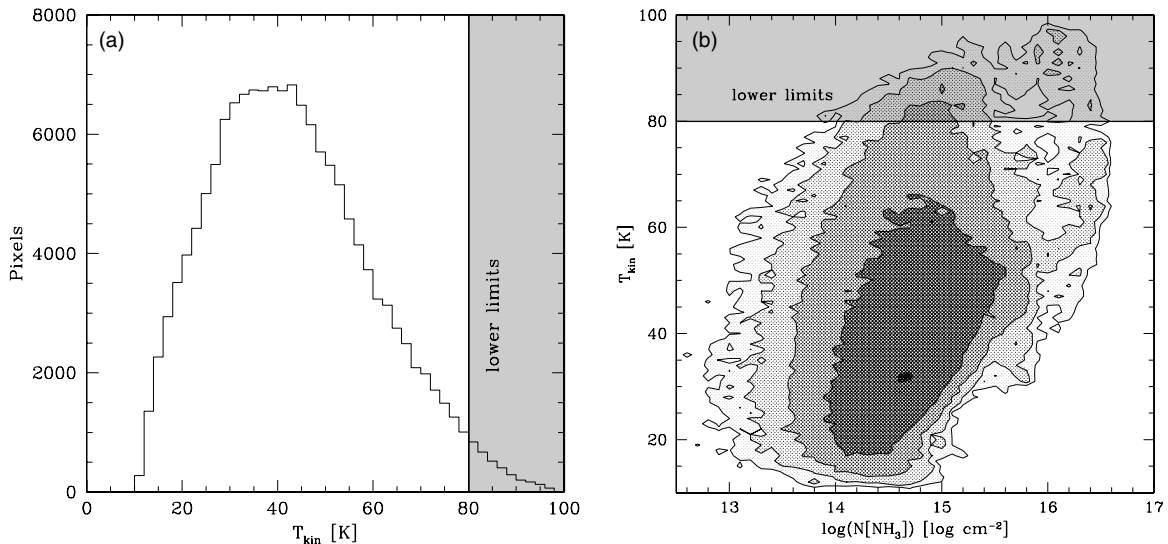


**Figure 11.** (a) The distribution of kinetic temperatures in our map. (b) Kinetic temperatures as a function of  $\text{NH}_3$  column density per pixel. All temperatures above 80 K need to be considered as lower limits.

Sgr B2 and at the position of the non-thermal arcs at about  $b \sim 0^\circ 15$ . This indicates that the structure might be described by an expansion with a velocity of  $\sim 30 \text{ km s}^{-1}$ . Signatures for an expansion were also detected in previous CO measurements by Sofue (1995), albeit with much larger expansion velocities. A comparison of our ammonia data with the intensity-weighted  $\text{N}_2\text{H}^+$  map presented in Jones et al. (2012) corroborates the view gained on the basis of the ammonia data alone, i.e., it appears to contradict the rotating ring picture. Our map, unfortunately, does not cover the region between Sgr A\* and Sgr C, which contains the other half of the 100 pc ring at  $\ell < 0^\circ$ .

#### 4.4. The Temperature Distribution of Molecular Clumps

Due to the filtering effect of the ATCA interferometer, we derive the temperature distribution of molecular clumps more or less directly, with little contribution from diffuse inter-clump gas. In Figure 11(a), we show the kinetic temperature distribution of all pixels in our map. The distribution peaks at about 38 K and has a FWHM of 43 K, spanning the 18–61 K range. We derive very few areas with a lower limit of kinetic temperatures of  $> 80$  K. Previous studies have detected high temperature components in the Galactic center molecular gas using single dish telescopes (e.g., Guesten et al. 1981; Huettemeister et al. 1993a; Rodríguez-Fernández et al. 2001; Ao et al. 2013; Mills & Morris 2013). It is very likely that the hot material is mostly diffuse and filtered out by our interferometric observations in combination with that our (1, 1) and (2, 2) lines are not sensitive to high temperatures. This pronounces the clumpier material which is substantially colder on average.

From Figure 8(b) we may see a trend that smaller clumps exhibit colder temperatures. A different view is shown in Figure 11 where we plot the logarithm of the total ammonia column density (cf. Section 4.1) to the derived kinetic temperature of the gas. The pixel by pixel correlation has been binned and logarithmic contours are shown. The plot confirms that gas at higher column density also tends to show a higher temperature. If the heating is external, one would expect it to affect clouds of all sizes to similar depths. Smaller clumps would thus be more thoroughly heated whereas larger clumps would be able to maintain a colder inner core. Since we see the opposite, we

may assume that most of the gas heating takes place internal to the individual clumps. If the star formation rate per molecular gas mass is roughly constant, larger clumps will contain more proto-stars, in particular more massive proto-stars. Those stars are the most likely candidates for internal heating. We hardly detect massive clumps with very low temperatures, or small clumps with large temperatures. Small clumps that do contain massive proto-stars may in fact dissipate relatively quickly, eluding their observation.

The Galactic center, however, is known to contain external heating sources such as cosmic rays, shocks, a strong UV field, X-ray sources, and dust. As explained above, most of the heating in the clumps is likely internal. But in some places the external heating may play a significant role, even for the smaller clumps. Notably, this includes the bow-shaped region from the thermal, arched filaments, through the high column density  $50 \text{ km s}^{-1}$  and  $20 \text{ km s}^{-1}$  clouds, in addition to the compact and dense Sgr B2 region which exhibits a strong temperature gradient (both traced by the yellow and red spots in Figure 8(a)). The bow-shaped region is close to Sgr A\*. Although the  $\text{CND}$  is cooler (see Section 4.6), the warmer gas may be influenced by activity of Sgr A\*, which may cause larger X-ray and cosmic ray fluxes, as well as shocks. Photo-dissociation region (PDR) effects may play a major role in the “mini-starburst” Sgr B2, which is also a place where the  $x_1$  and  $x_2$  orbits of the central stellar bar intersect. The resulting shocks might be an additional heating mechanism for the molecular gas in that area and can potentially explain the Sgr B2 temperature gradient that is hotter at larger Galactic longitude values.

#### 4.5. The Arches and Quintuplet Cluster Regions

Besides the Sgr B regions, young stellar clusters are visible all across the CMZ. Two of the most prominent, massive clusters are the Arches ( $0^\circ 121, 0^\circ 017$ ) and the Quintuplet ( $0^\circ 160, -0^\circ 059$ ) clusters displayed in Figure 12. The clusters have masses of  $\sim 10^4 M_\odot$  and are with ages of  $\sim 2$  Myr for the Arches and  $\sim 4$  Myr for the Quintuplet cluster (Figer et al. 1999) relatively young. The different ages may also be reflected in the dense gas map. Close to the Arches cluster, a large filament of dense molecular gas extends roughly parallel to the non-thermal

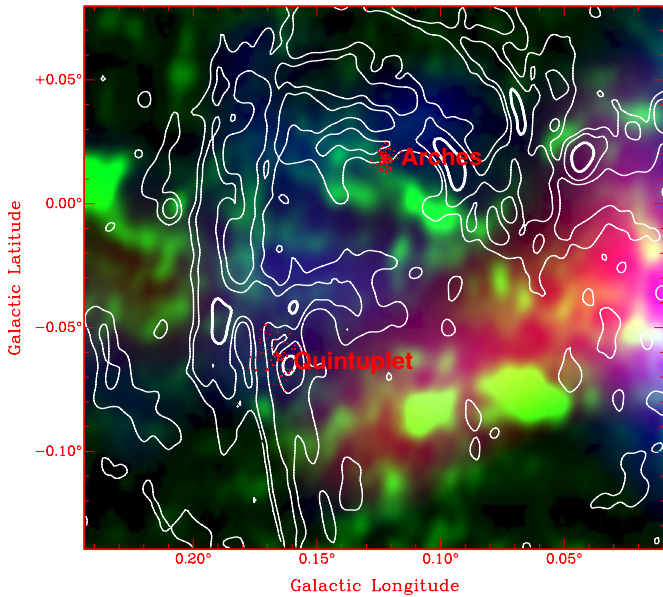


**Figure 12.** Multi-color composite of molecular gas close to the non-thermal filaments: Red: Integrated CO(4–3) emission, green: Ammonia (1, 1), blue: C I. Overlaid are the Arches and the Quintuplet stellar clusters in red contours and the 1.2 cm radio continuum in white (see Figure 2 for the contour spacing). The CO and C I data have been observed with the AST/RO south pole telescope (Martin et al. 2004).

(A color version of this figure is available in the online journal.)

radio continuum filament. The immediate surroundings of the Quintuplet cluster, however, are relatively clear of ammonia and may have dispersed over the lifetime of this cluster. The three-color composite map of the region in Figure 12 shows how different the distributions of the gas tracers are. CO emission (Martin et al. 2004) is brightest closer in the direction to the Galactic center and only little is visible in a roughly circular region that is defined by the radio arcs, the pistol/sickle and the thermal arched radio filaments that extend from the non-thermal arc to smaller Galactic longitudes. This region can be roughly described by a circle centered on  $(\ell, b) = (0^\circ:138, -0^\circ:007)$  and having a diameter of  $0^\circ:08$  (indicated by the cyan circle in Figure 4(b)). The region, almost entirely surrounded by radio continuum emission appears to be filled with [C I]  $^3P_0-^3P_1$  emitting gas (rest frequency: 492.161 GHz; data from Martin et al. 2004). [C I] is a well-known tracer for PDRs and this indicates that the gas is mainly ionized within this cavity. This is supported by the detection of Fe K $\alpha$  6.4 keV emission in the region (Wang et al. 2002, 2006; Tatischeff et al. 2012). The gas traced by ammonia is scattered all across that area. The main filaments, however, are close to the radio continuum emission toward the inside of the region. The two stellar clusters are also at the inner edge of the radio continuum emission. The ammonia channel maps (Figure 5) at this position show signatures that may be interpreted as an expanding structure, but the relative velocities could well be due to other motions, too. If it is expanding, the driving force could be provided by the gas traced by [C I]. This scenario would also explain why the morphology and kinematics of the NH<sub>3</sub> emission does not follow the overall sinusoidal pattern that is prominently observed by the molecular arcs between the shell (cyan circle in Figure 4(b)) and Sgr B2, which is continued south and north of Sgr A\* (Section 4.3).

The presence of strong [C I] emission also indicates PDR conditions and hence a higher ionizing flux and, since the [C I]

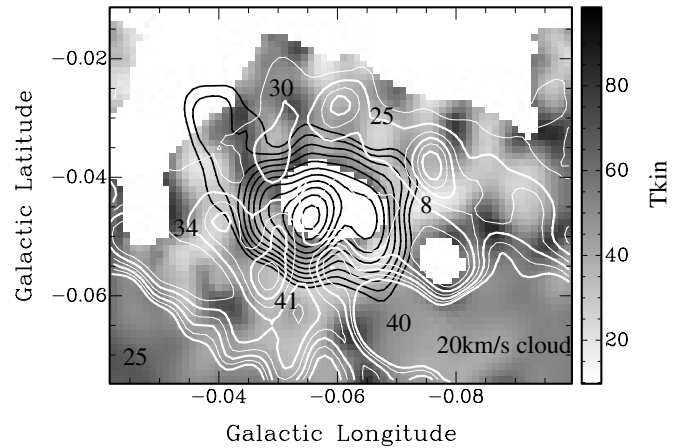


**Figure 13.** Circumnuclear disk around Sgr A\*. Shown are the contours of the NH<sub>3</sub>(1, 1) column density map in white contours (levels from  $10 \times 10^{13} \text{ cm}^{-2}$  in  $10 \times 10^{13} \text{ cm}^{-2}$  increments), and the 1.2 cm continuum outlining Sgr A\* and the mini-spiral in black contours. The grayscale image is the kinetic temperature map. Numbers indicate the peak velocity values at various positions. The 20 km s<sup>-1</sup> cloud is located toward smaller Galactic latitudes.

emission is widespread, a higher temperature. The temperature map of ammonia (Figure 8), however, shows values of  $T_{\text{kin}} \sim 40\text{--}60$  K which are only slightly enhanced compared to other, more quiet regions of the mapped area. The denser gas therefore appears to be well-shielded against heating from ionizing flux. If the picture of an expanding shell structure holds true, the distribution of the different gas tracers may thus indicate that dense gas forms a boundary layer that is filled with ionized and PDR gas (see also the discussion in Section 4.2). The dense gas layer is also where the Arches and Quintuplet clusters are located. The radio continuum is emitted from an additional sheet surrounding the dense gas that takes the role of the interface to the unaffected ISM. Substructures are observed close to the stellar clusters and within the radio continuum emission.

The more immediate environment of the Quintuplet cluster is relatively devoid of ammonia emission but has a local peak in [C I]. It also shows radio continuum emission aligned with the outer part of the structure. This emission forms the pistol/sickle region. The situation is less clear for the gas in the immediate surroundings of the Arches cluster. The Arches appears to be located on the rim of a cavity, that is centered on  $(\ell, b) \sim (0^\circ:107, 0^\circ:033)$  and filled with PDR gas. Since warm, ionized gas follows the path of least resistance, it may originate from the Arches cluster but then accumulates in this substructure.

#### 4.6. The Circumnuclear Disk

The CND around Sgr A\* is the most central position in our Milky Way at which substantial amounts of molecular gas are detected. The ring has been mapped in various dense molecular tracers, like HCN (e.g., Christopher et al. 2005; Montero-Castaño et al. 2009; Martín et al. 2012) and shows a characteristic diameter of an arcminute (or about 3 pc) with a total mass of  $\sim 10^6 M_\odot$  stored in various clumps (Christopher et al. 2005). A temperature map with NH<sub>3</sub> (1, 1) column density contours is shown in Figure 13. We detect a clumpy structure that is in broad agreement with the HCN observations. Herrnstein & Ho (2005) mapped the region in the ammonia lines with the Very Large Array. They detect an even clumpier distribution with their more extended array. With our shorter spacings, we are able to detect the most likely connection of the CND with

the 20 km s<sup>-1</sup> cloud and possibly the 50 km s<sup>-1</sup> cloud (see also McGary et al. 2001). The 20 km s<sup>-1</sup> cloud has a velocity gradient and at the position where it connects to the CNB, the value is about 40 km s<sup>-1</sup> (see Figure 13). From this level, the values roughly decrease in a clockwise direction around the CNB. This indicates that gas is fed from the 20 km s<sup>-1</sup> cloud to the CNB.

Given that the CNB is only  $\sim 1.5$  pc away from the supermassive black hole Sgr A\*, it is surprisingly cold. We detect kinetic temperatures between 25 K in the clumps and a maximum of  $\sim 70$  K in some inter-clump regions. Our values are much lower than single-dish measurements that derive a few hundred K for two regions of the CNB (e.g., Requena-Torres et al. 2012). This could indicate that the CNB is composed of clumpy cold and diffuse hot material as we are not sensitive to extended emission. The temperature structure of the clumps in the CNB is not significantly different from regions further away, e.g., in the molecular arcs (Section 4.3). As seen in Figure 8, the temperatures of the CNB are also lower than those in the warmer bow-shaped region described in Section 4.4. Cooling and shielding appears to be more efficient in the CNB, if the higher surrounding temperatures are caused by Sgr A\*.

## 5. SUMMARY

We observed the region between the supermassive black hole Sgr A\* and the massive star forming region Sgr B2 in our Milky Way with the ATCA in the ammonia (1, 1) and (2, 2) inversion lines ( $-0^{\circ}.2 \leq l \leq 0^{\circ}.8$ ;  $-0^{\circ}.13 \leq b \leq 0^{\circ}.07$ ). The interferometric data filters the clumpy structure that otherwise blends with a more diffuse component in single-dish observations. We find the following:

1. The dense gas is distributed in many filamentary structures with two prominent molecular arcs between Sgr A\* and Sgr B2. The dense molecular arcs are likely located on the “100 pc” ring that was recently detected in *Herschel* dust temperature maps.
2. Except for the extreme Sgr B2 region, the 1.2 cm radio continuum and ammonia emission are almost anti-coincident. This includes the continuum emitted from Sgr B1, the non-thermal arcs, the arched, thermal filaments, as well as the mini-spiral around Sgr A\*.
3. SCUBA 850  $\mu$ m data trace the dense ammonia gas very well, in an almost linear relationship. We see possible indications that a minimum amount of dust may be required for substantial amounts of ammonia to form and survive the encompassing UV radiation field.
4. A map of kinetic temperatures is constructed that is reasonably accurate in the 10–80 K range. For some of the gas, in particular gas close to Sgr B2 and in the vicinity of the 20 and 50 km s<sup>-1</sup> clouds and the arched, thermal filaments, we derive a lower limit of  $> 80$  K for the kinetic temperature.
5. The peak of the kinetic temperature distribution is at  $\sim 38$  K with a FWHM that spans 18–61 K. On average, larger clumps exhibit larger temperatures than smaller clumps. The dominating heating mechanism is thus likely internal, and possible sources could be proto-stars.
6. The molecular gas for the CNB immediately surrounding Sgr A\* with a radius of  $\sim 1.5$  pc is likely being supplied by the 20 km s<sup>-1</sup> cloud. The CNB is cooler than gas in the 20 km s<sup>-1</sup> and 50 km s<sup>-1</sup> clouds, and gas closer to the arched, thermal filaments.

7. The region close to the Arches and Quintuplet clusters shows signs for a layered structure with more diffuse PDR gas that is surrounded by dense ammonia clumps. Furthermore, the radio continuum filaments form an outer layer.

The Galactic center is an energetic region and understanding the dense gas clumps is key to understanding star formation in extreme conditions. The difference of the diffuse and dense gas components can be revealed by additional single dish observations. Finally it will be desirable to observe higher transitions over the full CMZ to obtain a map of a larger range of temperatures. For example, the NH<sub>3</sub>(2, 2) line has an energy of  $\sim 64$  K above ground, but the (3, 3), (6, 6), and (9, 9) levels are at  $\sim 123$  K,  $\sim 407$  K, and  $\sim 852$  K, respectively, and therefore trace much warmer gas. Other temperature tracers can be used to calibrate all methods against each other. The CMZ is also an important benchmark for comparisons with other galactic nuclei, near and far, active and quiet. Understanding the details of heating and cooling, star formation, active galactic nucleus feedback and gas transfer in the nearby CMZ is therefore indispensable to understand the role of nuclear regions for galaxy evolution at all cosmic epochs.

We thank James Aguirre for providing us access to re-reduced SCUBA data. The National Radio Astronomy Observatory is a facility of the National Science Foundation operated under cooperative agreement by Associated Universities, Inc. This research has made use of NASA’s Astrophysics Data System and the NASA/IPAC Extragalactic Database (NED) which is operated by the Jet Propulsion Laboratory, California Institute of Technology, under contract with the National Aeronautics and Space Administration.

## REFERENCES

- Alexander, R. D., Begelman, M. C., & Armitage, P. J. 2007, *ApJ*, 654, 907
- Amo-Baladr3n, M. A., Mart3n-Pintado, J., Morris, M. R., Muno, M. P., & Rodr3guez-Fern3ndez, N. J. 2009, *ApJ*, 694, 943
- Anantharamaiah, K. R., Pedlar, A., Ekers, R. D., & Goss, W. M. 1991, *MNRAS*, 249, 262
- Ao, Y., Henkel, C., Menten, K. M., et al. 2013, *A&A*, 550, A135
- Arendt, R. G., Stolovy, S. R., Ram3rez, S. V., et al. 2008, *ApJ*, 682, 384
- Babusiaux, C., & Gilmore, G. 2005, *MNRAS*, 358, 1309
- Bartko, H., Martins, F., Trippe, S., et al. 2010, *ApJ*, 708, 834
- Blitz, L., & Spergel, D. N. 1991, *ApJ*, 379, 631
- Cabrera-Lavers, A., Gonz3lez-Fern3ndez, C., Garz3n, F., Hammersley, P. L., & L3pez-Corredoira, M. 2008, *A&A*, 491, 781
- Carretti, E., Crocker, R. M., Staveley-Smith, L., et al. 2013, *Natur*, 493, 66
- Christopher, M. H., Scoville, N. Z., Stolovy, S. R., & Yun, M. S. 2005, *ApJ*, 622, 346
- Churchwell, E., & Hollis, J. M. 1983, *ApJ*, 272, 591
- Crocker, R. M., Jones, D. I., Aharonian, F., et al. 2011, *MNRAS*, 413, 763
- Danby, G., Flower, D. R., Valiron, P., Schilke, P., & Walmsley, C. M. 1988, *MNRAS*, 235, 229
- Figer, D. F., Kim, S. S., Morris, M., et al. 1999, *ApJ*, 525, 750
- Ghez, A. M., Salim, S., Weinberg, N. N., et al. 2008, *ApJ*, 689, 1044
- Gillessen, S., Eisenhauer, F., Trippe, S., et al. 2009, *ApJ*, 692, 1075
- Guesten, R., Walmsley, C. M., & Pauls, T. 1981, *A&A*, 103, 197
- Handa, T., Omodaka, T., Nagayama, T., Bebe lahak, H., & Matsuyama, N. 2006, *JPhCS*, 54, 42
- Henkel, C., Mauersberger, R., Peck, A. B., Falcke, H., & Hagiwara, Y. 2000, *A&A*, 361, L45
- Herrnstein, R. M., & Ho, P. T. P. 2005, *ApJ*, 620, 287
- Ho, P. T. P., & Townes, C. H. 1983, *ARA&A*, 21, 239
- Huettmeister, S., Wilson, T. L., Bania, T. M., & Mart3n-Pintado, J. 1993a, *A&A*, 280, 255
- Huettmeister, S., Wilson, T. L., Henkel, C., & Mauersberger, R. 1993b, *A&A*, 276, 445

- Jones, P. A., Burton, M. G., Cunningham, M. R., et al. 2012, *MNRAS*, **419**, 2961
- Kim, S. S., Saitoh, T. R., Jeon, M., et al. 2011, *ApJL*, **735**, L11
- Lang, C. C., Morris, M., & Echevarria, L. 1999, *ApJ*, **526**, 727
- Liu, S., & Melia, F. 2001, *ApJL*, **561**, L77
- Longmore, S. N., Rathborne, J., Bastian, N., et al. 2012, *ApJ*, **746**, 117
- Lu, J. R., Do, T., Ghez, A. M., et al. 2013, *ApJ*, **764**, 155
- Martin, C. L., Walsh, W. M., Xiao, K., et al. 2004, *ApJS*, **150**, 239
- Martín, S., Martín-Pintado, J., Montero-Castaño, M., Ho, P. T. P., & Blundell, R. 2012, *A&A*, **539**, A29
- Martín, S., Requena-Torres, M. A., Martín-Pintado, J., & Mauersberger, R. 2008, *ApJ*, **678**, 245
- Martín-Pintado, J., de Vicente, P., Rodríguez-Fernández, N. J., Fuente, A., & Planesas, P. 2000, *A&A*, **356**, L5
- Mauersberger, R., Henkel, C., Wilson, T. L., & Walmsley, C. M. 1986, *A&A*, **162**, 199
- McGary, R. S., Coil, A. L., & Ho, P. T. P. 2001, *ApJ*, **559**, 326
- Mehring, D. M., Palmer, P., & Goss, W. M. 1995, *ApJS*, **97**, 497
- Mills, E. A. C., & Morris, M. R. 2013, *ApJ*, **772**, 105
- Molinari, S., Bally, J., Noriega-Crespo, A., et al. 2011, *ApJL*, **735**, L33
- Montero-Castaño, M., Herrnstein, R. M., & Ho, P. T. P. 2009, *ApJ*, **695**, 1477
- Morris, M., & Serabyn, E. 1996, *ARA&A*, **34**, 645
- Nord, M. E., Lazio, T. J. W., Kassim, N. E., et al. 2004, *AJ*, **128**, 1646
- Oka, T., Hasegawa, T., Sato, F., Tsuboi, M., & Miyazaki, A. 1998, *ApJS*, **118**, 455
- Ott, J., Henkel, C., Braatz, J. A., & Weiß, A. 2011, *ApJ*, **742**, 95
- Ott, J., Weiss, A., Henkel, C., & Walter, F. 2005, *ApJ*, **629**, 767
- Pierce-Price, D., Richer, J. S., Greaves, J. S., et al. 2000, *ApJL*, **545**, L121
- Protheroe, R. J., Ott, J., Ekers, R. D., Jones, D. I., & Crocker, R. M. 2008, *MNRAS*, **390**, 683
- Purcell, C. R., Longmore, S. N., Walsh, A. J., et al. 2012, *MNRAS*, **426**, 1972
- Reid, M. J., Menten, K. M., Zheng, X. W., Brunthaler, A., & Xu, Y. 2009, *ApJ*, **705**, 1548
- Requena-Torres, M. A., Güsten, R., Weiß, A., et al. 2012, *A&A*, **542**, L21
- Rodríguez-Fernández, N. J., Combes, F., Martín-Pintado, J., Wilson, T. L., & Apponi, A. 2006, *A&A*, **455**, 963
- Rodríguez-Fernández, N. J., Martín-Pintado, J., Fuente, A., et al. 2001, *A&A*, **365**, 174
- Sault, R. J., Teuben, P. J., & Wright, M. C. H. 1995, in ASP Conf. Ser. 77, *Astronomical Data Analysis Software and Systems IV*, ed. R. A. Shaw, H. E. Payne, & J. J. E. Hayes (San Francisco, CA: ASP), 433
- Sofue, Y. 1995, *PASJ*, **47**, 551
- Stark, A. A., Martin, C. L., Walsh, W. M., et al. 2004, *ApJL*, **614**, L41
- Su, M., Slatyer, T. R., & Finkbeiner, D. P. 2010, *ApJ*, **724**, 1044
- Tatischeff, V., Decourchelle, A., & Maurin, G. 2012, *A&A*, **546**, A88
- Ungerechts, H., Winnewisser, G., & Walmsley, C. M. 1986, *A&A*, **157**, 207
- Walmsley, C. M., & Ungerechts, H. 1983, *A&A*, **122**, 164
- Wang, Q. D., Dong, H., & Lang, C. 2006, *MNRAS*, **371**, 38
- Wang, Q. D., Gotthelf, E. V., & Lang, C. C. 2002, *Natur*, **415**, 148
- Weiß, A., Neininger, N., Henkel, C., Stutzki, J., & Klein, U. 2001, *ApJL*, **554**, L143
- Yusef-Zadeh, F., Hewitt, J. W., & Cotton, W. 2004, *ApJS*, **155**, 421